

Finite Temperature Properties of Magnetic Polarons in Two-Dimensional Quantum Antiferromagnets

Eigenschaften von magnetischen Polaronen in
zweidimensionalen Quanten-Antiferromagneten bei
endlicher Temperatur



Masterarbeit der Fakultät für Physik
der
Ludwig-Maximilians-Universität München

Toni Benedikt Guthardt

Betreuer:

Prof. Dr. Jan von Delft

München November 29, 2024

Abstract

Due to significant progress in quantum gas microscopes in recent years, there is a rapidly growing interest in real space properties of single mobile dopands created in correlated antiferromagnet (AFM) on a square lattice. In addition, angle-resolved photoemission spectroscopy (ARPES) has revealed particularly interesting spectral properties of mobile dopands in cuprates. However, a theoretical description remains extremely challenging, even when restricting to simple toy-models. As a consequence previous numerical simulations have been limited to $T = 0$. However, in order to link simulations to cold-atom experiments, numerical calculations at finite temperature are required. Here, we numerically study both the real-time properties as well as the spectral features of a single mobile hole in the 2D t - J model at finite temperature and draw a comparison to features observed at $T = 0$. We find that a three stage process of hole motion, which was reported at $T = 0$, is valid even at finite temperature. However, already at low temperatures, the hole velocity at long times is not simply proportional to the spin coupling, contrary to the $T = 0$ behaviour. For the high-temperature behavior at strong coupling regime, remarkably good agreement was found with subdiffuse behavior up to intermediate temperatures. Furthermore, we find magnetic polaron peaks in the spectral function up to $T \approx 1J$, demonstrating that magnetic polarons are robust with respect to temperature. Their dispersion relation remains qualitatively unchanged with temperature in the region away from (π, π) as long as magnetic polarons are present. Instead of a strong suppression of spectral weight around (π, π) , which was observed for $T = 0$, we find non-vanishing spectral weight and even indications of spin-charge separation already at low temperatures.

Contents

1	Introduction	6
2	Methods	9
2.1	Formalism and MPS Basics	9
2.1.1	Motivation	10
2.1.2	MPS Basics	11
2.1.3	Evaluation of expectation values	13
2.1.4	Application of MPO to MPS	13
2.1.5	Compression of an MPS	14
2.1.6	Projector formalism	16
2.2	Time-dependent variational principle (TDVP)	19
2.2.1	Derivation	19
2.2.2	Errors	22
2.3	Controlled-bond-expansion (CBE)	23
2.4	Global Krylov time evolution	26
2.4.1	Derivation	27
2.4.2	Errors and Numerical Efficiency	29
2.4.3	Use in combination with MPS	29
2.4.4	Caveats: Loss of Orthogonality	30
2.4.5	Variational Orthogonalization	31
2.5	Purification	33
2.5.1	Ancilla space backward time evolution	36
2.5.2	Two-site disentangler	37
2.6	MPO Implementation	39
2.6.1	Conceptual discription	39
2.6.2	Combination with tensor networks	44
2.6.3	Summary	47
3	Results	48
3.1	Real time dynamics	48
3.1.1	Background	48
3.1.2	Varying temperature	50
3.1.3	Varying the coupling ratio	50
3.1.4	Subdiffusion behavior at infinite temperature	52
3.1.5	Hole density and spin across system	54
3.1.6	Next nearest neighbor spin correlations	55
3.1.7	Nearest neighbor spin correlations	57
3.1.8	Spinon spreading	58
3.2	Spectral properties	58
3.2.1	Background	61
3.2.2	General observations at finite temperature	62
3.2.3	Temperature resistance of polarons	63

3.2.4	Dispersion relations of ground and first excited polaron states	63
3.2.5	Suppression of the spectral weight around $\mathbf{k} = (\pi, \pi)$	64
3.2.6	Analysis of behavior around $\mathbf{k} = (0, 0)$	64
4	Conclusion	65
	Acknowledgements	68
A	Spectral function	69
A.1	Symmetrization	69
B	Spin correlations in equilibrium	69
C	Convergence	69
	Bibliography	73

1 Introduction

The comprehension of the strongly correlated nature of diverse classes of materials has constituted a significant challenge in recent years. Despite the existence of precise physical laws that describe the underlying behavior [1], a precise solution for complex systems remains elusive. At the core of this challenge lies the necessity to describe real materials with a vast number of particles, as well as the exponential growth of the computational effort required as the system size increases. In order to address the challenge of dealing with a large number of interacting particles, various approximate schemes have been employed in the past, wherein the interaction is only considered to a limited extent. In such cases, the system is typically described from the perspective of a single particle, with interactions introduced perturbatively. A prominent example of this is Landau's Fermi-liquid theory [2]. While these methods have proven effective in describing electrical resistivity and more complex phenomena such as conventional superconductivity, they are inadequate for systems exhibiting strong electron interactions. Unfortunately, strong electron interactions typically give rise to pronounced correlations, which are thought to underlie a number of intriguing quantum effects, including high-temperature superconductivity [3, 4] and the fractional quantum Hall effect [5]. It is therefore evident that new methods are required to tackle the problem of simulating realistic many-body electron systems. As a direct numerical approach, the so-called 'exact diagonalization' (ED) is employed to obtain eigenvectors of the many-body Hamiltonian describing the system [6]. While ED is relatively straightforward to implement, it does not address the issue of exponentially growing complexity with system size. Consequently, it is typically limited to small system sizes, which can be particularly problematic for systems exhibiting long-ranged correlations.

Another highly successful approach is to stochastically treat the physical system under consideration. Such methods are collectively referred to as 'quantum Monte Carlo' (QMC) techniques [7–9] and can be utilized to sample the partition function even in the presence of strong interactions. Although this method has proven to be effective in treating a wide range of systems, including those with large system sizes, it has been demonstrated to require exponentially increasing computational resources with increasing system size when handling frustrated magnets or fermionic systems. The origin of this behavior can be attributed to the phenomenon known as the 'sign problem' [10]. This term refers to the situation in which the weights of certain system configurations become negative or complex, rendering them unable to be interpreted as classical probabilities [11]. As an alternative to QMC, which is not constrained by an inherent sign problem, so-called 'tensor network techniques' [12–14] are frequently employed. In this approach, the wavefunction of a system is expressed through a network of interconnected tensors, effectively constructing a tensor network. The advent of the density matrix renormalization group (DMRG) [15, 16] marked a pivotal moment in the evolution of these techniques, as it enabled the efficient computation of the ground state of a system in the form of a special

one-dimensional tensor network, known as a matrix product state (MPS). Being only limited by the entanglement in the wavefunction, tensor networks enable the simulation of large size strongly correlated systems. Therefore, they represent an ideal candidate to study the physics of cuprate superconductors, which has been an area of intensive research over the recent years.

The parent compound of cuprate superconductors is believed to be a two-dimensional Heisenberg antiferromagnet (AFM) [17]. In addition, it is generally assumed that an interplay between hole motion and antiferromagnetism is at the heart of high-temperature superconductivity in cuprates [18]. Therefore, it is of great interest to study the behavior of a single mobile charge carrier in an antiferromagnetic spin background.

In a quasi-1 dimensional system, angle-resolved photoemission spectroscopy (ARPES) [19–21] has revealed spin-charge separation by the observation of a broad continuum instead of discrete quasi particle peaks [22–28]. However, in two-dimensional, doped, quantum AFMs, APRES spectra have revealed long-lived magnetic polarons [29–52]. This observation has been further backed up by theoretical calculations at $T = 0$ that were performed in clean toy models, such as the t - J model [53, 54]. However, the behaviour at finite temperature is not yet fully understood.

Previous experiments using ARPES, as well as theoretical studies have investigated the formation of a so-called magnetic polaron, which is created when a single moving hole distorts the surrounding Néel spin background. In the conventional magnetic polaron picture, the polaron can be understood as a cloud of correlated magnons dressing the hole.

The motion of a hole, which is directly linked to an interplay of spin and charge, is intuitively described in real space. However, a major part of research has been focused on the frequency and momentum space, since they are most directly probed in solid state experiments. Due to significant progress in quantum gas microscopy in recent years [55–64], there is a rapidly growing interest in real space properties. It has been shown that a parton picture, first suggested by Béran et al. [65], for describing the magnetic polaron is able to capture the relevant physics qualitatively [66]. Here, a magnetic polaron consists of a holon, carrying the charge, which is connected by a chain of displaced spins with a spinon, carrying the spin [18, 53]. In one of the simplest approximate descriptions of a magnetic polaron in the parton picture, the so-called frozen spin approximation (FSA) is used, which considers only charge fluctuations along strings of displaced spins and leaves the wavefunction of the surrounding spins unaffected by hole hopping [51, 53, 67].

It is generally accepted that the Fermi-Hubbard-model provides an good starting point for a theoretical description of cuprates [68–70]. At strong coupling, it can be mapped to the t - J model

$$\hat{H} = -t \sum_{\langle \mathbf{i} \mathbf{j} \rangle, \sigma} \mathcal{P}(\hat{c}_{\mathbf{i}, \sigma}^\dagger \hat{c}_{\mathbf{j}, \sigma} + h.c.) \mathcal{P} + J \sum_{\langle \mathbf{i} \mathbf{j} \rangle} (\mathbf{S}_{\mathbf{i}} \cdot \mathbf{S}_{\mathbf{j}} - \frac{n_{\mathbf{i}} n_{\mathbf{j}}}{4}), \quad (1)$$

where the first term denotes the hopping of the hole with strength t and the second

term represents the spin-exchange interactions with coupling constant $J = 4t^2/U$. Note that \mathcal{P} projects onto the space with at most one fermion per site and we neglected a three site term [71] in Eq. (1).

Despite the apparent simplicity of this model, theoretical predictions and numerical simulations have proven challenging. As a consequence, previous theoretical calculations of hole dynamics have been limited to $T = 0$ behavior.

Quantum gas microscopy (QGM) represents a promising tool to bridge the gap between experiment and theoretical simulation. By employing this technique, it is possible to perform large-scale two-dimensional simulations and to study both real-space and time properties. As QGM operates at finite temperature, it enables access to the finite temperature spectral function in cold atom experiments offering complementary insights to ARPES experiments [72, 73]. These finite-temperature simulations are a first step towards understanding the intriguing finite-temperature phases observed in cuprates. Hence, it is essential to perform numerical calculations at finite temperature in order to provide guidance for QGM at finite temperature.

In this thesis we perform the numerical simulation of finite temperature properties of a single hole in a cylinder with length $L_x = 18$ and width $L_y = 4$ moving according to the t - J model. All simulations were prepared by calculating the thermal equilibrium of the t - J -model at half-filling. The result was an insulating antiferromagnet. We then modified it by removing a single electron, thus initializing the motion of a magnetic polaron. Our work provides two major advances: (i) We provide valuable insights into the real time dynamics of holes at finite temperature. (ii) We enhance our understanding of magnetic polarons, by the calculation of spectra at finite temperature.

The main findings can be summarized as follows: First, we observe that the main stages of hole motion reported at $T = 0$ are valid even at finite temperature. However, contrary to the $T = 0$ behaviour, the hole velocity observed for times larger than $1/J$ is not proportional to the spin coupling J . This can be seen already at temperatures $T = 0.5J$ and above. Second, in the strong coupling regime, a remarkably good agreement with subdiffusive behaviour exists at temperatures going down to $T = 2J$. Third, we report the presence of magnetic polaron peaks up to $T \approx 1J$. This is consistent with the temperature up to which non-vanishing AFM correlations are present at long times, $\tau \approx 6[1/J]$. This is an important observation, since it demonstrates that magnetic polarons are robust with respect to temperature. Furthermore, we find that their dispersion relation remains qualitatively unchanged with temperature in the region away from (π, π) as long as magnetic polarons are present. Fourth, we observe non-zero spectral weight and even indications of spin-charge separation around (π, π) for temperatures larger than $T = 0.5J$. This is in contrast to the $T = 0$ behaviour, which reported a strong suppression of spectral weight in that region [54].

The structure of this thesis is as follows: In Sec. 2 we present the details of our tensor network methods, which have been used to perform the numerical simulations. We begin by motivating a tensor network approach and introducing the basics of matrix-

product states (MPS). This is followed by a detailed derivation of the time-evolution algorithms used. We conclude this section by discussing the treatment of finite temperature and our method of implementing matrix-product operators (MPOs). In the main part of this thesis, Sec. 3, we present the results of our research. We start with an analysis of the results of our real-time dynamics at finite temperature: First an introduction to the background knowledge is presented, then we illustrate the behavior of the dynamics when varying temperature and coupling ratio. Finally, we conclude the part on dynamics with a discussion of spin correlations. In the second part of our results, we highlight the spectral properties at finite temperature and perform a detailed comparison with important features observed at $T = 0$. We close by discussing implications of our work and future research directions.

2 Methods

This section will provide a comprehensive explanation of the combination of algorithms that has been employed in our computations. In order to calculate the thermal equilibrium of the t - J -model at half-filling we used the density matrix renormalization group (DMRG) [74, 75] in the language of matrix-product-states (MPSs) [12]. This approach was adapted to finite temperatures via a purification scheme [76–78] and enhanced by the use of disentanglers [79]. The subsequent motion of the hole was simulated by combining two versions of MPS-based time evolution algorithms [80]. Although the entanglement physically only spreads locally around the location of the quench, it is encoded via the virtual bonds of the MPS, which spans the entire lattice. This is why we began the time evolution with a single step of the more expensive, but global Krylov scheme [81–83]. The rest of the time evolution was performed via the local, but less expensive time-dependent-variational-principle (TDVP) algorithm [84, 85]. This procedure was improved by the use of a backwards-time-evolution scheme [86–88], which allowed us to reach longer times without additional approximations. In all of the above algorithms, we also used the controlled bond expansion [89, 90], which effectively performs two-site optimizations at one-site costs. We will now proceed with an introduction to the fundamental concepts of matrix product states.

2.1 Formalism and MPS Basics

This section is mainly based on [12, 79, 80, 89–91] and introduces the basics of Matrix Product States (MPS) as well as more advanced concepts that will be used later to explain the algorithms used. We begin by motivating a tensor network approach to the description of quantum systems.

2.1.1 Motivation

Entanglement represents a foundational phenomenon in quantum mechanics. It describes the inherent interdependence of different degrees of freedom within a quantum system, rendering them incapable of being measured independently. To understand this phenomenon, we partition the Hilbert space \mathcal{H} into A and B parts $\mathcal{H} = \mathcal{H}_A \otimes \mathcal{H}_B$. Employing a technique known as the Schmidt decomposition, which is unique up to degeneracies, we can represent a pure state $|\psi\rangle \in \mathcal{H}$ as

$$|\psi\rangle = \sum_{\alpha} \lambda_{\alpha} |\alpha\rangle_A \otimes |\alpha\rangle_B, \quad (2)$$

where the states $\{|\alpha\rangle_A\}$ and $\{|\alpha\rangle_B\}$ form an orthonormal basis of the Hilbert spaces \mathcal{H}_A and \mathcal{H}_B , respectively, and the Schmidt coefficients λ_{α} are non-negative. It can be shown that the squared 2-norm $\| |\psi\rangle \|_2^2$ is equal to the sum over squares of singular values $\sum_{\alpha} (\lambda_{\alpha})^2$ of the state. Consequently, it follows that $\sum_{\alpha} \lambda_{\alpha}^2 = 1$ for a normalized state. We may now proceed to define the reduced density matrix of A as

$$\hat{\rho}_A := \text{Tr}_B \hat{\rho}, \quad \text{with } \hat{\rho} = |\psi\rangle \langle \psi|, \quad (3)$$

which enables us to measure the entanglement between A and B in terms of the entanglement entropy $S_{A/B}$, which is defined as

$$S_{A/B} = -\text{Tr}_A \hat{\rho}_A \log_2 \hat{\rho}_A. \quad (4)$$

Inserting Eq. (2) into Eq. (4) it is easy to see that $S_{A/B}$ can be expressed as

$$S_{A/B} = -\sum_{\alpha} \lambda_{\alpha}^2 \log_2 \lambda_{\alpha}^2. \quad (5)$$

Consequently, one can directly extract information regarding the entanglement of two subsystems from the Schmidt decomposition. For instance, in the absence of entanglement between two subsystems, the Schmidt decomposition only yields a single term with $\lambda_1 = 1$.

Area law A general quantum state in the Hilbert space \mathcal{H}_A obeys the so-called 'volume law'. This implies that the entanglement increases in proportion to the volume of each subsystem. In contrast, for a gapped and local Hamiltonian \hat{H} the ground state (GS) $|\psi_0\rangle$ follows an 'area law' [92–94], whereby the entanglement entropy grows proportional to the area of the boundary between the two subsystems. In this context, the boundary is defined as the set of sites that connect the subsystem to the environment through operator action. For the purposes of this discussion, we will consider a system with a linear dimension of L . In the case of a one-dimensional (1D) tensor network laid through our system, such as Matrix Product States (MPS),

see Sec. 2.1.2, the entanglement entropy is therefore constant in 1D, linear in L in 2D and quadratic in L in 3D. A detailed proof for 1D systems is given in [94].

The area law exerts a profound influence on the numerical cost of adequately encoding entanglement in the tensor network description of a GS. This can be observed in two distinct ways: (i) It has been demonstrated that states that satisfy the area law contain their entire weight in only a few Schmidt states. This provides an extremely useful method of compressing quantum states by truncating the Schmidt decomposition, which is directly related to the matrix product state representation of a quantum state. (ii) It is possible to derive bounds on the number of basis states D required to encode the entanglement in our system. This is achieved by starting from the entanglement entropy S and using bases in which ρ_A and ρ_B are diagonal. Making use of Eq. (4) we obtain

$$S = - \sum_{\alpha=1}^D w_{\alpha} \log_2 w_{\alpha}, \quad (6)$$

where w_{α} are eigenvalues of ρ_A .

Clearly, this is maximal if $w_{\alpha} = \frac{1}{D}$, resulting in

$$S \leq - \sum_{\alpha=1}^D \frac{1}{D} \log_2 \frac{1}{D} = \log_2 D. \quad (7)$$

Upon further reformulation, we arrive at

$$2^S \leq D. \quad (8)$$

Combined with the special case of the area law, the reduced density matrix bond dimension D is independent of system size in 1D systems. This property enables the efficient encoding of ground state entanglement. In 2D and 3D, however, the numerical cost increases exponentially in L when using MPS to represent our system.

2.1.2 MPS Basics

Having motivated the use of tensor networks in the context of gapped 1D systems, we will now proceed to introduce some of the basic concepts of MPS. Considering a chain of L sites, where each site is labelled by l , a general quantum state $|\psi\rangle$ in the Hilbert space \mathcal{H} is defined as

$$|\psi\rangle = \psi^{\sigma} |\sigma\rangle \quad (9)$$

with $|\sigma\rangle = |\sigma_1\rangle |\sigma_2\rangle \dots |\sigma_L\rangle$ and each σ_l being a local basis state. This state can be

expressed as an open boundary matrix-product-state (MPS),

$$\begin{aligned} \psi^\sigma &= [M_1]_{1,\alpha_1}^{\sigma_1} [M_2]_{\alpha_1,\alpha_2}^{\sigma_2} \cdots [M_L]_{\alpha_{L-1},1}^{\sigma_L}, \\ &= \begin{array}{c} \times \quad M_1 \quad M_2 \quad \quad \quad \quad \quad \quad \quad M_L \quad \times \\ \quad \circ \\ \quad | \\ \quad \sigma_1 \quad \sigma_2 \quad \quad \quad \quad \quad \quad \quad \sigma_{L-1} \quad \sigma_L \\ \quad \alpha_1 \quad \alpha_2 \quad \quad \quad \quad \quad \quad \quad \alpha_{L-1} \end{array} . \end{array} \quad (10)$$

The notation $[M_l]_{\alpha_{l-1},\alpha_l}^{\sigma_l}$ represents a three-dimensional array of complex or real numbers, referred to as a 'tensor'. Connected bonds represent indices that are summed over, and are therefore referred to as 'virtual bonds'. The bond dimension, denoted by D_l , is a parameter that characterises the dimensionality of the virtual bond and is typically constrained by a maximum bond dimension D . The physical bonds σ_l are of dimension d . The outermost bonds, indicated by a cross, are dummy bonds with dimension $D_0 = D_L = 1$. It should be noted that the bond dimension required to exactly represent the quantum state grows exponentially with the system size. Nevertheless, we have motivated the fruitfulness of this approximation as a consequence of the area law, see Sec. 2.1.1. The transformation of the wavefunction into the form of Eq. (10) can be readily accomplished through the iterative application of truncated QR decompositions to the wavefunction.

The gauge freedom inherent to the MPS representation allows the MPS wavefunction to be transformed into a variety of forms. One of the most significant forms is the so-called 'canonical form' with respect to either a bond connecting sites l and $l+1$ or an 'orthogonality center' at site l

$$\psi^\sigma = \begin{array}{c} \times \quad A_1 \quad \quad \quad A_{l-1} \quad C_l \quad B_{l+1} \quad B_L \quad \times \\ \quad \diagdown \quad \diagdown \quad \diagdown \quad \circ \quad \diagup \quad \diagup \quad \diagup \\ \quad \sigma_1 \quad \quad \quad \sigma_{l-1} \quad \sigma_l \quad \sigma_{l+1} \quad \quad \quad \sigma_L \end{array} , \quad (11)$$

which is displayed here. The triangles situated to the left of the orthogonality center are left isometries, i.e. $[A_l^\dagger]_{\alpha'\bar{\alpha}}^\sigma [A_l]_{\bar{\alpha}\alpha}^\sigma = [\mathbb{1}_l]_{\alpha'\alpha}$. The triangles on the right represent right isometries, i.e. $[B_l]_{\alpha\bar{\alpha}}^\sigma [B_l^\dagger]_{\bar{\alpha}\alpha'}^\sigma = [\mathbb{1}_{l-1}]_{\alpha\alpha'}$. It should be noted that the diagonals of the left and right isometries point in opposite directions. The circle represents the tensor that is the orthogonality center. The orthogonality center can be shifted using singular value decompositions (SVDs).

An analogue procedure can be used for the representation of any operator $\hat{O} = |\sigma\rangle O^{\sigma\sigma'} \langle\sigma'|$ in terms of a matrix product operator (MPO)

$D' = D\omega \gg D$. Therefore the direct application is not desirable. In the following we will present a more efficient alternative.

Zip-up method As an alternative to the direct application of an MPO to an MPS, the zip-up method [80] represents an efficient approach. The fundamental premise is that the MPO merely distorts the canonical form of the MPS to a limited extent. Consequently, a moderate degree of truncation can be employed during the contraction without significant loss of information. At the first site, the MPO tensor is simply contracted with the corresponding right-normalised tensor, B , in a manner analogous to the direct application of a MPO to a MPS

$$[M_1]_{1,\alpha_1,1,\nu_1}^{\sigma'_1} = \sum_{\sigma_1} [W_1]_{1,\nu_1}^{\sigma_1,\sigma'_1} [B_1]_{1,\alpha_1}^{\sigma_1}. \quad (15)$$

Here the two dummy legs, identified by index '1', can be readily fused to an leg bearing the index '2'. The subsequent step is to apply an SVD, which will yield

$$\text{SVD}([M_1]_{2,\alpha_1,\nu_1}^{\sigma'_1}) \approx \sum_{s_1,s'_1} [A_1]_{2,s_1}^{\sigma'_1} [S]_{s_1,s'_1} [V^\dagger]_{s'_1,\alpha_1,\nu_1}. \quad (16)$$

The final step is to multiply both tensors S and V^\dagger on the right into the next tensor B , which will then be split up afterwards. Accordingly, the subsequent M comprises the following elements

$$[M_2]_{2,s_1,\alpha_2,\nu_2}^{\sigma'_2} = \sum_{\sigma_2,s'_1,\alpha_1,\nu_1} [S]_{s_1,s'_1} [V^\dagger]_{s'_1,\alpha_1,\nu_1} [W_2]_{\nu_1,\nu_2}^{\sigma_2,\sigma'_2} [B_2]_{\alpha_1,\alpha_2}^{\sigma_2}. \quad (17)$$

This process is iterated until the right side of the system is reached and the MPS is in left canonical form. For an illustration of the main steps, see Fig. 1. The primary cost, which is resulting from the singular value decomposition (SVD), is given by $\mathcal{O}(D^3dw)$. It should be noted that the leg s_1 in the case of M_2 is usually a leg of dimension D if we are situated at the center of the system.

2.1.5 Compression of an MPS

Given that numerous operations on an MPS result in an increase in its bond dimension—such as those observed in MPO-MPS applications, see Sec. 2.1.4—it is frequently necessary to truncate an MPS to a desired bond dimension. In particular, the objective is to identify a state $|\phi\rangle$ with a lower bond dimension that provides an optimal approximation of the state $|\psi\rangle$ so that it minimizes the Hilbert space distance F

$$F = || |\psi\rangle - |\phi\rangle ||. \quad (18)$$

The most direct approach is to perform an iterative sweep through the MPS, truncating each bond individually using SVDs. Nevertheless, selecting the optimal choice

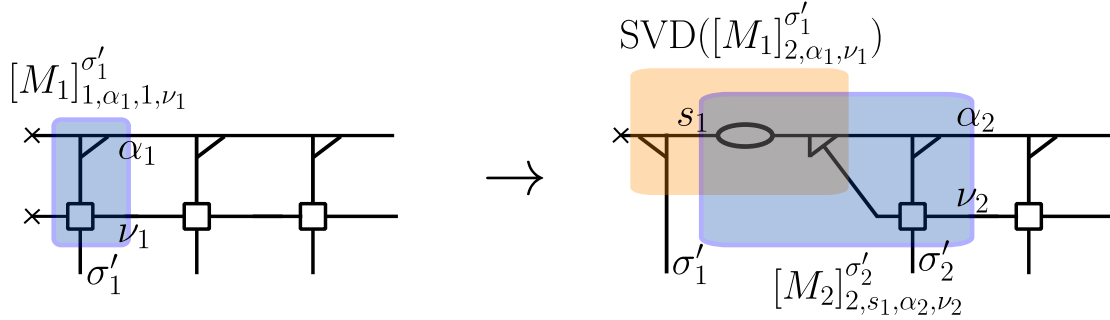


Figure 1: Illustration of the zip-up method. The process begins with a state in right canonical form and concludes with a state in left canonical form. The most important steps described in Sec. 2.1.4 are displayed. The colored areas indicate the objects to be contracted and the objects to which an SVD is to be applied.

for each individual bond does not necessarily yield the global optimum. Consequently, alternative optimization techniques are more beneficial. In the following, we will introduce the so-called 'variational compression' [80] that we used in our calculations.

Variational compression In order to utilize a more sophisticated algorithm than direct truncation and sweeping through the system, we present an iterative sweeping scheme. The objective is to sweep through the system and identify the locally optimal tensor at each site or set of sites. This approach increases the probability of identifying a globally optimal tensor.

The goal is to identify the optimal MPS $|\phi\rangle$, which is the most accurate representation of the initial state $|\psi\rangle$, given a truncated bond dimension. This yields the minimization problem

$$\| |\psi\rangle - |\phi\rangle \|^2 = \langle \psi | \psi \rangle - \langle \psi | \phi \rangle - \langle \phi | \psi \rangle + \langle \phi | \phi \rangle. \quad (19)$$

It is important to note that the selection of an appropriate initial guess state for $|\phi\rangle$ can have a significant impact on the convergence speed of the compression process. Typically, the state obtained by sweeping the system and performing local truncation via SVDs is the most effective. By fixing all tensors except a set of s adjacent tensors, it is possible to optimise the tensors $A_l \cdots A_{l+s-1}$ of $|\phi\rangle$ by differentiating Eq. (19) with respect to $A_l^\dagger \cdots A_{l+s-1}^\dagger$

$$\frac{\delta}{\delta A_l^\dagger \cdots A_{l+s-1}^\dagger} (\langle \psi | \psi \rangle - \langle \psi | \phi \rangle - \langle \phi | \psi \rangle + \langle \phi | \phi \rangle) = \frac{\delta}{\delta A_l^\dagger \cdots A_{l+s-1}^\dagger} (\langle \phi | \phi \rangle) - \langle \phi | \psi \rangle \stackrel{!}{=} 0. \quad (20)$$

If we consider our state to be in canonical form with orthogonality center at site l , Eq. (20) further simplifies into

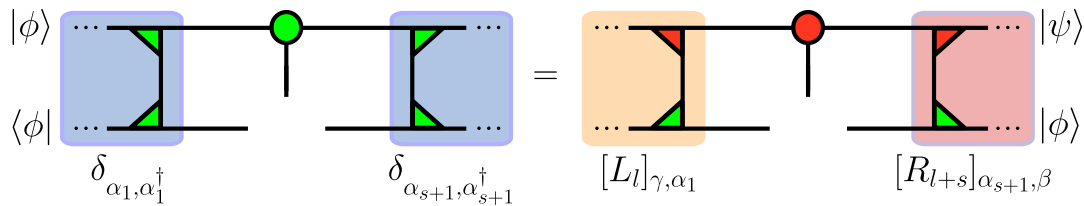


Figure 2: Illustration of the central equation Eq. (21) defining variational compression. The tensor network is presented for the case $s = 1$. The colored areas indicate either the identity resulting from contracting left or right isometries, or alternatively, the LR environments.

$$A_l \cdots A_{l+s-1} = \sum_{\alpha_1 \cdots \alpha_{s+1}} [L_l]_{\gamma, \alpha_1} [B_l]_{\alpha_1, \alpha_2}^{\sigma_l} \cdots [B_{l+s-1}]_{\alpha_s, \alpha_{s+1}}^{\sigma_{l+s-1}} [R_{l+s}]_{\alpha_{s+1}, \beta} , \quad (21)$$

where B represent the tensors of $|\psi\rangle$ and the environment tensors LR are defined as the overlaps between the states $\langle\phi|$ and $|\psi\rangle$. For an illustration of Eq. (21) as well as an illustration of how the environments LR are computed, see Fig. 2. It is important to note that the environment tensors LR do not have to be recomputed from scratch at each stage of the sweep; they can be successively updated as the system is swept. As usual, it is beneficial to use a two-site ($s = 2$) scheme in preference to a single-site ($s = 1$) scheme. This allows for the bond dimension to be adjusted and new symmetry sectors to be explored if necessary. As is always the case, this approach entails the truncation of the wavefunction after a local step in order to maintain a manageable bond dimension.

2.1.6 Projector formalism

In the following we want to introduce the so-called 'projector formalism', which will be used in subsequent sections. The left and right isometries introduced above can be used to define left $|\psi_{i\alpha}^K\rangle$ and right $|\phi_{i\alpha}^K\rangle$ 'kept' states. The wavefunctions $\psi_{i\alpha}^K$ ($\phi_{i\alpha}^K$) of these left (right) kept states can be represented as

$$\psi_{i\alpha}^K = \begin{array}{c} \times \quad A_1 \quad \quad \quad A_{\bar{l}} \\ \diagdown \quad \diagup \quad \diagdown \quad \diagup \\ \hline \alpha \end{array} \quad (22)$$

$$\phi_{i\alpha}^K = \alpha \begin{array}{c} B_{\bar{l}} \quad \quad \quad B_L \\ \diagup \quad \diagdown \quad \diagup \quad \diagdown \\ \hline \times \end{array} , \quad (23)$$

where the letter 'K' represents the kept space. The designation "kept" is applied to the states in question because they build our MPS. The following discussion will

$$P_l^b = P_{l,l+1}^{KK} = \begin{array}{c} \times \quad \times \quad \times \\ \diagdown \quad \diagup \quad \diagdown \quad \diagup \\ \text{---} \text{---} \text{---} \text{---} \text{---} \\ \diagup \quad \diagdown \quad \diagup \quad \diagdown \\ \times \quad \times \quad \times \end{array} \quad \begin{array}{c} \times \quad \times \quad \times \\ \diagdown \quad \diagup \quad \diagdown \quad \diagup \\ \text{---} \text{---} \text{---} \text{---} \text{---} \\ \diagup \quad \diagdown \quad \diagup \quad \diagdown \\ \times \quad \times \quad \times \end{array} \quad (29)$$

$$P_l^{1s} = P_{l-1,l+1}^{KK} = \begin{array}{c} \times \quad \times \quad \times \\ \diagdown \quad \diagup \quad \diagdown \quad \diagup \\ \text{---} \text{---} \text{---} \text{---} \text{---} \\ \diagup \quad \diagdown \quad \diagup \quad \diagdown \\ \times \quad \times \quad \times \end{array} \quad \begin{array}{c} | \\ | \\ | \end{array} \quad \begin{array}{c} \times \quad \times \quad \times \\ \diagdown \quad \diagup \quad \diagdown \quad \diagup \\ \text{---} \text{---} \text{---} \text{---} \text{---} \\ \diagup \quad \diagdown \quad \diagup \quad \diagdown \\ \times \quad \times \quad \times \end{array} . \quad (30)$$

It should be noted that this definition also allows us to derive the following useful relation

$$P_l^{1s} P_{l+1}^{1s} = P_l^b. \quad (31)$$

The next step is to construct the so-called 1s tangent space projector P^{1s} , which we will need in Sec. 2.2. The tangent space projector P^{1s} projects on the 1s tangent space. This space is spanned by all one-site variations of $|\psi\rangle$, wherein only a single site undergoes a change. One might suggest that it be constructed via $\sum_{\bar{l}=1}^L P_{\bar{l}}^{1s}$. However, this approach is not viable since the summands are not mutually orthogonal. Accordingly, an orthogonalisation procedure, akin to Gram-Schmidt, is employed: We define $P_{\bar{l}<}^{1s}$ by projecting out the overlap of $P_{\bar{l}}^{1s}$ with $P_{\bar{l}\pm 1}^{1s}$ from $P_{\bar{l}}^{1s}$

$$P_{\bar{l}<}^{1s} := P_{\bar{l}}^{1s} (\mathbb{1}_V - P_{\bar{l}\pm 1}^{1s}). \quad (32)$$

Explicitly writing we get,

$$P_{\bar{l}<}^{1s} = P_{\bar{l}}^{1s} - P_{\bar{l}}^b = P_{\bar{l},\bar{l}+1}^{DK} \begin{array}{c} \times \quad \times \quad \times \\ \diagdown \quad \diagup \quad \diagdown \quad \diagup \\ \text{---} \text{---} \text{---} \text{---} \text{---} \\ \diagup \quad \diagdown \quad \diagup \quad \diagdown \\ \times \quad \times \quad \times \end{array} \quad \begin{array}{c} \times \quad \times \quad \times \\ \diagdown \quad \diagup \quad \diagdown \quad \diagup \\ \text{---} \text{---} \text{---} \text{---} \text{---} \\ \diagup \quad \diagdown \quad \diagup \quad \diagdown \\ \times \quad \times \quad \times \end{array} \quad (33)$$

$$P_{\bar{l}>}^{1s} = P_{\bar{l}}^{1s} - P_{\bar{l}-1}^b = P_{\bar{l}-1,\bar{l}}^{KD} \begin{array}{c} \times \quad \times \quad \times \\ \diagdown \quad \diagup \quad \diagdown \quad \diagup \\ \text{---} \text{---} \text{---} \text{---} \text{---} \\ \diagup \quad \diagdown \quad \diagup \quad \diagdown \\ \times \quad \times \quad \times \end{array} \quad \begin{array}{c} \times \quad \times \quad \times \\ \diagdown \quad \diagup \quad \diagdown \quad \diagup \\ \text{---} \text{---} \text{---} \text{---} \text{---} \\ \diagup \quad \diagdown \quad \diagup \quad \diagdown \\ \times \quad \times \quad \times \end{array}, \quad (34)$$

where we made use of Eq. (31) and the completeness relation Eq. (27). This provides us with the requisite formalism for the construction of the tangent space projector

$$P^{1s} := \sum_{\bar{l}=1}^{l'-1} P_{\bar{l}<}^{1s} + P_{l'}^{1s} + \sum_{\bar{l}=l'+1}^L P_{\bar{l}>}^{1s}. \quad (35)$$

Now with Eq. (33) and Eq. (34) we can bring this into a form that we can use later comfortably

$$\begin{aligned}
P^{1s} &= \sum_{\bar{l}=1}^L P_{\bar{l}}^{1s} - \sum_{\bar{l}=1}^{L-1} P_{\bar{l}}^b \\
&= \sum_{\bar{l}=1}^L \left(\text{Diagram 1} \right) - \sum_{\bar{l}=1}^{L-1} \left(\text{Diagram 2} \right).
\end{aligned}
\tag{36}$$

This concludes the overview of the fundamental concepts that are essential for an understanding of the algorithms that will be presented in the following sections.

2.2 Time-dependent variational principle (TDVP)

This section is mainly based on [79, 80, 84, 85]. There are a number of different approaches to performing time evolution for MPS, each with its own set of advantages and disadvantages. Typical approaches range from direct approximation of the time evolution operator $\hat{U}(\delta) = e^{-i\hat{H}\delta}$ to the approximation of the action of $\hat{U}(\delta)$ on $|\psi\rangle$ or the local solution of the time-dependent Schrödinger equation (TDSE).

In the following, we present an algorithm that aims at the latter and has a 'single site' (1s) and a 'two site' (2s) variant. As the 1s variant is the most relevant to our purposes, we will focus on it and only briefly introduce the 2s variant at the end for the sake of completeness.

2.2.1 Derivation

The time-dependent variational principle (TDVP) represents a local time evolution method for MPS. The main idea is that by evolving the MPS forward by only a small time step dt , the time evolved state lives in the 1s tangent space of the MPS. The 1s tangent space is spanned by all single-site variations of $|\psi\rangle$, whereby only one site is altered. In other words, it is assumed that non-local information is insignificant with regard to the evolution of an observable. Therefore, the procedure is as follows: The initial step is to project our Schrödinger equation into this space, after which the time evolution can be performed within it.

Starting with the Schrödinger equation for the MPS

$$\frac{\delta}{\delta t} |\psi\rangle = -i\hat{H} |\psi\rangle,
\tag{37}$$

we can observe that the left side of Eq. (37) already lives in 1s tangent space, as is particularly evident if we consider $|\psi\rangle$ in bond canonical form. Subsequently, the left side of Eq. (37) can be expressed as

$$\frac{\delta}{\delta t} |\psi\rangle = \sum_{\nu=1}^l \text{---} \overset{\dot{A}_\nu}{\circ} \text{---} + \sum_{\nu=l+1}^L \text{---} \overset{\dot{B}_\nu}{\circ} \text{---}. \quad (38)$$

It is evident that each of the terms in Eq. (38) differs from $|\psi\rangle$ by exactly one site. In contrast, the right side is clearly not in 1s tangent space, given that the Hamiltonian is applied to the state. Next we apply the 1s tangent space projector P^{1s} , see Sec. 2.1.6, to the Schrödinger equation, resulting in a series of coupled equations

$$\begin{aligned} \frac{\delta}{\delta t} |\psi\rangle &= -i\hat{P}^{1s}\hat{H}|\psi\rangle \\ &= -i\sum_{l=1}^L \hat{P}_l^{1s}\hat{H}|\psi\rangle + i\sum_{l=1}^{L-1} \hat{P}_l^b\hat{H}|\psi\rangle. \end{aligned} \quad (39)$$

Considering Eq. (39), it is obvious that an exact solution is not possible. To proceed, one finds an approximate solution by decoupling the series of equations, which results in L forward-evolving equations

$$\frac{\delta}{\delta t} |\psi\rangle = -i\hat{P}_l^{1s}\hat{H}|\psi\rangle \quad (40)$$

and L-1 backward-evolving equations

$$\frac{\delta}{\delta t} |\psi\rangle = i\hat{P}_l^b\hat{H}|\psi\rangle. \quad (41)$$

By applying 1s $\psi_{l-1}^{K\dagger} \otimes \phi_{l+1}^{K\dagger}$ and bond maps $\psi_l^{K\dagger} \otimes \phi_{l+1}^{K\dagger}$ respectively onto our series of equations, we finally arrive at

$$i\frac{\delta C_l(t)}{\delta t} = \hat{H}_l^{1s}C_l(t) \quad (42)$$

$$i\frac{\delta \Lambda_l(t)}{\delta t} = -\hat{H}_l^b\Lambda_l(t). \quad (43)$$

Here the effective 1s (bond) Hamiltonians \hat{H}_l^{1s} (\hat{H}_l^b) are defined as the 'partial' expectation values of the state $|\psi\rangle$ with the Hamiltonian \hat{H} leaving either one site (bond) open, resulting in

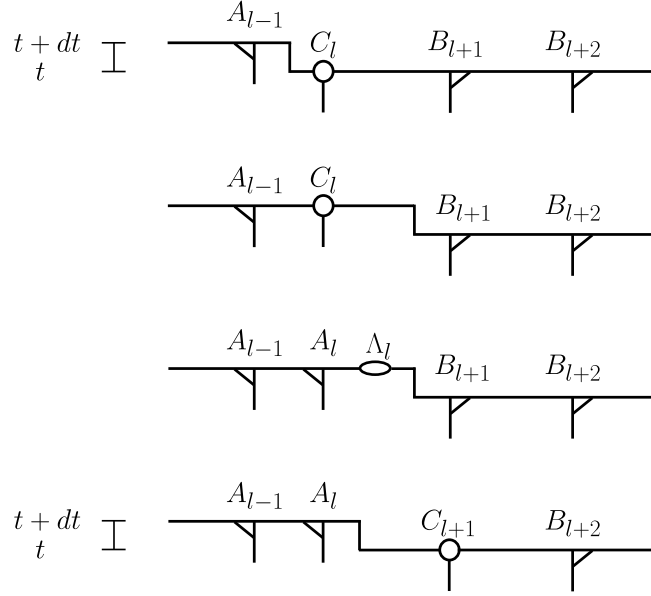


Figure 3: Graphical representation of the process of sweeping from left to right through the system. The initial step is to evolve the local orthogonality center forward in time. Subsequently, the orthogonality center is split by QR or SVD decomposition, and the resulting bond tensor is evolved backwards in time. Then we move to the next site and iterate the process.

$$\hat{H}_l^{1s} = \begin{array}{c} \text{Diagram of } \hat{H}_l^{1s} \text{ tensor} \\ \text{---} \end{array} \quad (44)$$

$$\hat{H}_l^b = \begin{array}{c} \text{Diagram of } \hat{H}_l^b \text{ tensor} \\ \text{---} \end{array} \quad (45)$$

In practice, one sweeps through the system and solves the local time evolution steps Eq. (42) and Eq. (43) at each site individually. At each local step, we first evolve the orthogonality center forward in time, then perform a QR or SVD decomposition, and then evolve the bond tensor backward in time. For an illustration see Fig. 3.

The initial decoupling scheme gives rise to a first-order integrator with an error per unit time that is proportional to the time step size δ . Typically, the system is swept first from left to right and then from right to left at a time step that is at half the initial time step δ . This corresponds to a second-order integrator that reduces the error to $\mathcal{O}(\delta^2)$ for unit time.

Each of these local time steps can be performed exactly. Typically, a local Krylov method is employed for this purpose. It should be noted that, as the projection onto the tangent space is performed prior to the actual time evolution, both the norm and the energy of the state are conserved.

As previously stated, the scheme presented above is a so-called 1s scheme (1TDVP). A significant drawback of this 1s scheme is that it lacks the capability to explore different symmetry sectors. To address this issue, a 2s variant (2TDVP) of the scheme can be readily derived from the 1s scheme. It should be noted, however, that this scheme is not as conceptually clean as the 1s scheme, since states with different ranges of quantum numbers live in different manifolds. In this procedure, a two-site tensor is forward evolved, and then it is split into two single-site tensors using SVD. Subsequently, one of the two local 1s tensors resulting from the SVD, positioned in the sweep direction, is subjected to backward evolution. By splitting the two-site tensor into two single-site tensors with SVD, the bond dimension of the connecting bond will grow. This allows us to explore new quantum sectors; however, the bond dimension typically has to be truncated to a manageable value afterwards. However, due to the truncation of the two-site tensor, the norm and energy of the state are no longer conserved. Furthermore, this scheme is considerably more expensive than the single-site scheme. In 1TDVP the main cost is $\mathcal{O}(D^3dw)$, whereas in 2TDVP it is $\mathcal{O}(D^3d^2w)$. The main cost is due to the application of the Hamiltonian to the local 1s or 2s tensor.

2.2.2 Errors

The TDVP is riddled with four significant errors.

(i) The projection of the time-dependent Schrödinger equation (TDSE) onto the tangent space of limited bond dimension results in an error $\Delta_p^{1s,2s}$, with

$$\Delta_p^{1s,2s} := \|(1 - \hat{P}^{1s,2s})\hat{H}\psi(t)\|. \quad (46)$$

This error is particularly large when the MPS under consideration has a relatively small bond dimension. As this projection occurs prior to the time evolution, it is not possible for it to violate energy conservation or alter the norm of the state. An approximate estimate for the magnitude of this error can be made: In the event that the n-site variance of the state is large, then (n-1)TDVP will be inaccurate.

(ii) A sweep through the system can be understood as a sequential solution of multiple coupled TDSEs, each describing a local time evolution. This results in an error of the order of $\mathcal{O}(\delta^2)$ for unit time and of the order of $\mathcal{O}(\delta^3)$ per time step when a second-order integrator is employed. Furthermore, this error is amplified in the presence of bond dimensions that are relatively small.

(iii) This error is specific to the 2TDVP and is related to the SVD. It is typically necessary to truncate the bond dimension in order to maintain a manageable level of complexity, which introduces a truncation error. This error can be observed by

maintaining a record of the discarded weight, which is defined as the sum over the squares of the singular values that are discarded during an SVD.

(iv) The final source of error arises from the inaccurate solution of the local equations. It is straightforward to maintain a low level of this error by utilising an adequate number of Krylov steps in the local Krylov method.

It is also crucial to recognise that the time step size δ affects the four errors in different ways: The projection error and the truncation error are both relatively insensitive to the time step size of a single time step. A reduction in the time step size will result in an increased number of time steps being required to achieve the desired time, which will in turn result in an amplified projection and truncation error.

Conversely, the finite time-step error and the error resulting from the inaccurate solution of local equations reduce as the number of time-steps increases. It is therefore essential to exercise caution when selecting the time step size δ to ensure that all four errors are adequately balanced.

In my calculations I use a scheme that combines the high accuracy of the 2s scheme with the low computational cost of a 1s scheme. This is achieved by combining the 1s scheme with a technique known as Controlled Bond Expansion (CBE), which will be discussed in greater detail next.

2.3 Controlled-bond-expansion (CBE)

This section is based on [89–91]. The goal of the controlled-bond-expansion (CBE) is to enhance a single-site scheme, such as 1TDVP, in order to achieve 2s accuracy while maintaining 1s cost.

As previously outlined in the formalism section, see Sec. 2.1, an MPS can be expressed in terms of isometries, which can be used to define the kept and discarded spaces. In order to comprehend the objective of the CBE, it is essential to examine the part that a two-site scheme captures and a one-site scheme does not. In the construction of the Krylov space required to evolve the system forward locally, we apply the effective Hamiltonian (denoted as either \hat{H}_t^{1s} or \hat{H}_t^{2s}) to a one-site (1TDVP) or two-site tensor (2TDVP). Subsequent application of a unitary map to some of the

open bonds then yields

$$\begin{aligned}
 \text{1-site} \quad \begin{array}{c} \text{---} \\ \text{---} \\ \text{---} \\ \text{---} \\ \text{---} \end{array} & \xrightarrow{\text{unitary}} \begin{array}{c} \text{---} \\ \text{---} \\ \text{---} \\ \text{---} \\ \text{---} \end{array} = \begin{array}{c} \text{---} \\ \text{---} \\ \text{---} \\ \text{---} \\ \text{---} \end{array} \oplus \begin{array}{c} \text{---} \\ \text{---} \\ \text{---} \\ \text{---} \\ \text{---} \end{array} \\
 \text{1-site} \quad \begin{array}{c} \text{---} \\ \text{---} \\ \text{---} \\ \text{---} \\ \text{---} \end{array} & \xrightarrow{\text{unitary}} \begin{array}{c} \text{---} \\ \text{---} \\ \text{---} \\ \text{---} \\ \text{---} \end{array} = \begin{array}{c} \text{---} \\ \text{---} \\ \text{---} \\ \text{---} \\ \text{---} \end{array} \oplus \begin{array}{c} \text{---} \\ \text{---} \\ \text{---} \\ \text{---} \\ \text{---} \end{array} \\
 \text{2-site} \quad \begin{array}{c} \text{---} \\ \text{---} \\ \text{---} \\ \text{---} \\ \text{---} \\ \text{---} \end{array} & \xrightarrow{\text{unitary}} \begin{array}{c} \text{---} \\ \text{---} \\ \text{---} \\ \text{---} \\ \text{---} \\ \text{---} \end{array} = \begin{array}{c} \text{---} \\ \text{---} \\ \text{---} \\ \text{---} \\ \text{---} \\ \text{---} \end{array} \oplus \begin{array}{c} \text{---} \\ \text{---} \\ \text{---} \\ \text{---} \\ \text{---} \\ \text{---} \end{array} \oplus \begin{array}{c} \text{---} \\ \text{---} \\ \text{---} \\ \text{---} \\ \text{---} \\ \text{---} \end{array} \oplus \begin{array}{c} \text{---} \\ \text{---} \\ \text{---} \\ \text{---} \\ \text{---} \\ \text{---} \end{array}
 \end{aligned} \tag{47}$$

It is readily observable in Eq. (47) that the part that is omitted by the 1s scheme is the discarded-discarded (DD) subspace, which is represented by the filled black triangles.

Alternatively, one may consider the perspective that CBE in combination with TDVP aims to minimize the 2s contribution to the projection error Δ_p^{1s} . In the following we will refer to this quantity as $\Delta_p^{2\perp}$, which is defined as the two-site contribution to the projection error

$$\Delta_p^{2\perp} = \|\hat{P}^{2s}(1 - \hat{P}^{1s})\hat{H}\psi(t)\| = \sum_{l=1}^{L-1} \left\| \begin{array}{c} \text{---} \\ \text{---} \\ \text{---} \\ \text{---} \\ \text{---} \\ \text{---} \end{array} \right\|^2. \tag{48}$$

Note that this alternative perspective leads to the same conclusion previously stated in Eq. (47), namely that the 2s contribution is comprised of the DD sectors.

The fundamental insight of CBE is that $\hat{H}_l^{2s}\psi_l^{2s}$ possesses considerable weight only on a small subspace of the large DD space. It is therefore sufficient to expand a bond only by this small relevant subspace. This insight is employed to compute a so-called 'truncated isometry' \tilde{A}_l^{tr} , which carries the relevant part of the DD subspace and has a dimension of only $\tilde{D} < D$ on the MPS bond, in contrast to the much larger \bar{D} .

The method for calculating the truncated isometry is referred to as 'shrewd selection' [89]. The object to be minimized in the shrewd selection is obtained from both the equation Eq. (47) and the equation Eq. (48). It is referred to as the cost function C , which is defined as

$$C = \left\| \begin{array}{c} \text{---} \\ \text{---} \\ \text{---} \\ \text{---} \\ \text{---} \\ \text{---} \end{array} - \begin{array}{c} \text{---} \\ \text{---} \\ \text{---} \\ \text{---} \\ \text{---} \\ \text{---} \end{array} \right\|, \tag{49}$$

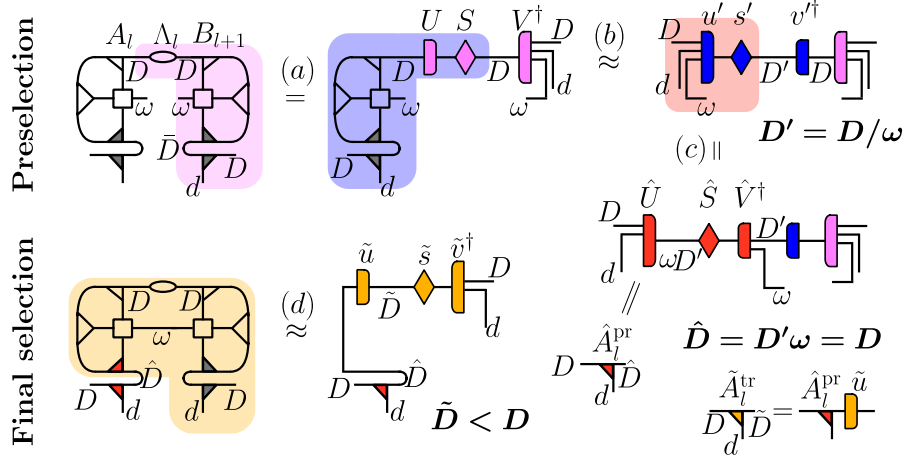


Figure 4: Shrewd selection process. The matching colours serve to indicate the SVD input and output. The small letters of the SVD output indicate truncation during SVD. Preselection: (a) SVD without truncation and open MPO bond. (b) SVD with truncation down to $D' = D/\omega$. (c) The truncated MPS bond and MPO bond are to be fused into a bond of size $\hat{D} = D$. Final selection: (d) SVD with truncation and a closed MPO bond, which reduces the bond dimension to $\tilde{D} < D$.

where the orange triangles represent the truncated isometries that are the subject of our computation. The optimal minimization of C could be achieved via SVD, although this would entail a 2s cost. The shrewd selection represents an efficient method for minimizing this quantity, while requiring only 1s cost. The shrewd selection is comprised of two steps: The initial stage of the process is the so-called 'preselection'. In this step, the central MPS bond is truncated down from D to D' . This has the consequence that the full complement \bar{A}_l is replaced by a preselected complement \hat{A}_l^{pr} with an already reduced image dimension \hat{D} , with $\hat{D} = D'\omega$. The final selection entails a further truncation of \hat{A}_l^{pr} with closed MPO bond to yield the final result \tilde{A}_l^{tr} , with image dimension $\tilde{D} < D$. It should be noted, that for the shrewd selection to remain at a 1s cost, it is necessary that $\hat{D} = D$. Accordingly, one selects $D' = D/\omega$. For further details on the shrewd selection, see Fig. 4.

Having now acquired the requisite knowledge to compute the truncated isometry, the subsequent step is to provide an explanation of the process for combining it with single-site TDVP. The procedure for utilising CBE for a local TDVP step is as follows: (i) The truncated isometry is computed through shrewd selection. (ii) Subsequently, the isometry and the orthogonality center involved in the local time evolution as well as the effective Hamiltonian are expanded using this truncated isometry. (iii) Finally, a local 1s step is performed with the regular 1s scheme in the expanded space.

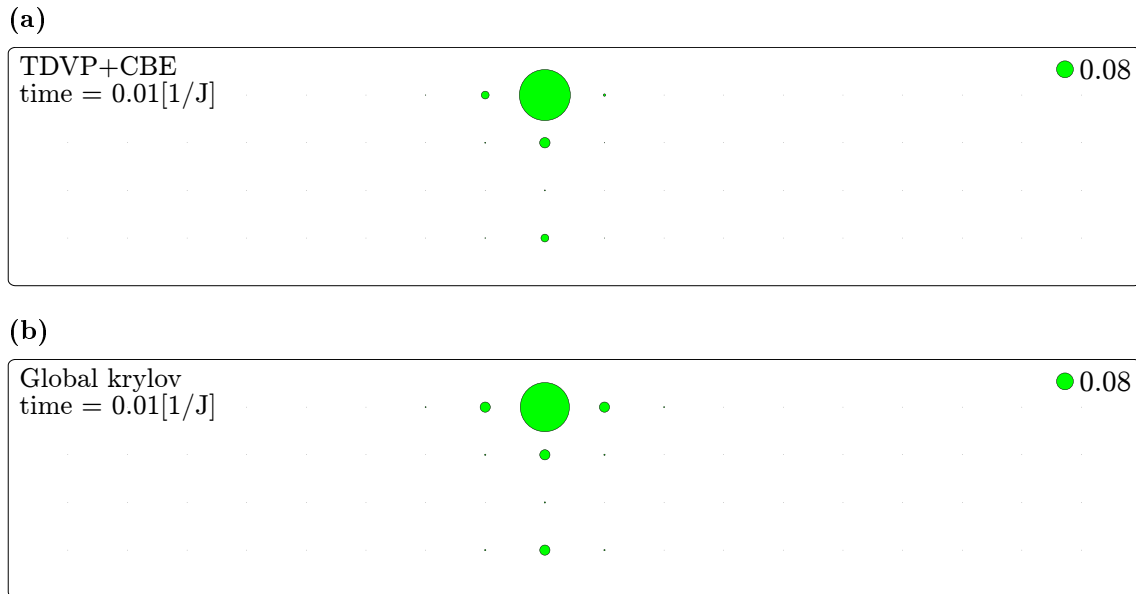


Figure 5: Illustration of the necessity of utilising Global Krylov for the initial time step. Initially, the ground state of the t - J model at $t/J = 2$ was computed. Subsequently, an electron was removed from a central site, and the resulting dynamics were plotted over the entire lattice. We display the hole density in a 4 by 18 cylinder after a single short time step. The size of the green circles represents the strength of the hole density. Notably, the site with the maximum hole density corresponds to the initial hole location. (a) The first time evolution step was performed with the TDVP. (b) The first time evolution step was performed with the Global Krylov scheme. Given the asymmetric propagation of the hole in (a) as opposed to the symmetric spreading in (b), it can be concluded that the Global Krylov scheme performs with significantly higher accuracy at the first time step.

2.4 Global Krylov time evolution

This section is based on [80,95] and presents an additional time evolution method that is required due to a subtle weakness of the TDVP that we use for the majority of the time evolution. At the outset of the time evolution, a hole is created in the ground state of the 2D system under consideration. However, upon the creation of this hole, the bond dimension remains fixed, despite the necessity for a generally higher bond dimension to encode the increase in entanglement in our system. As TDVP is a local method, the bond dimension is increased bond by bond as the state is evolved forward. Consequently, the correct behaviour is not captured immediately after the hole is added. To address this issue, we implemented a global time evolution algorithm, which performs the initial time evolution step, after which TDVP is used to complete the evolution. An illustration of the error produced without the use of global Krylov at the initial time step can be seen in Fig. 5.

The global Krylov method is a Krylov subspace method. In the context of time

evolution, the objective is to approximate the action of the exact time evolution operator $\hat{U}^{exact}(\delta)$ on the state $|\psi(t)\rangle$ as a whole. Consequently, we avoid manipulating the time evolution operator $\hat{U}^{exact}(\delta)$ on its own. It is noteworthy that the global algorithm presented below is highly analogous to the local Krylov solver used to solve the local time step in TDVP, see Sec. 2.2. In the following, we derive the algorithm in a way that is independent of MPS.

2.4.1 Derivation

We begin by introducing the Krylov subspace K_N of a Hamiltonian \hat{H} with an initial state $|\psi\rangle$ as the span of the vectors $\{|\psi\rangle, \hat{H}|\psi\rangle, \dots, \hat{H}^{N-1}|\psi\rangle\}$. The initial stage of the process is to construct the Krylov subspace by generating a set of Krylov vectors $|\nu_0\rangle, |\nu_1\rangle, \dots, |\nu_{N-1}\rangle$ that span the Krylov space: The initial state with norm 1 is set as the first Krylov state. Subsequently, an iterative process is employed: The most recent Krylov vector $|\nu_{i-1}\rangle$ is then subjected to the action of the Hamiltonian \hat{H} , resulting in the generation of a state with a significantly larger bond dimension. Subsequently, this temporary state is orthonormalised with respect to all previous Krylov vectors, thereby defining the next Krylov vector $|\nu_i\rangle$. It should be noted that, in exact arithmetic with the aforementioned construction it would be sufficient to orthonormalise only with respect to the two most recent Krylov vectors. However, due to rounding errors, it is typically necessary to orthogonalise with respect to all previous vectors. Having constructed our Krylov space, the question remains as to how we can best approximate the time evolution $\hat{U}^{exact}(\delta)|\psi(t)\rangle$. The Krylov method attempts to identify the element in K_N that provides the optimal approximation to the time evolution, i.e.

$$\hat{U}^{exact}(\delta)|\psi(t)\rangle \approx \arg \min_{|u\rangle \in K_N} \||u\rangle - \hat{U}^{exact}(\delta)|\psi(t)\rangle\| := |\psi(t + \delta)\rangle. \quad (50)$$

In order to achieve this, one defines the projector on K_N

$$\hat{P}_N = \sum_{i=0}^{N-1} |\nu_i\rangle \langle \nu_i| \quad (51)$$

$$\equiv V_N^\dagger V_N, \quad (52)$$

where the matrices V_N and V_N^\dagger store the Krylov vectors and operate as maps from Hilbert space \mathcal{H} to Krylov space. Subsequently, the solution to the minimization problem, see Eq. (50), is given by

$$|\psi_N(t + \delta)\rangle = \hat{P}_N^\dagger \hat{U}^{exact}(\delta) \hat{P}_N |\psi(t)\rangle. \quad (53)$$

It should be noted that, thus far, no approximations have been made under the assumption that $N = \dim \mathcal{H} \equiv N_{\mathcal{H}}$. As a final step, the Taylor expansion of $\hat{U}^{exact}(\delta)$ is employed, which results in

$$|\psi_{N_{\mathcal{H}}}(t + \delta)\rangle = \sum_{i=0}^{N_{\mathcal{H}}-1} |\nu_i\rangle \langle \nu_i| e^{-i\delta\hat{H}} \sum_{i'=0}^{N_{\mathcal{H}}-1} |\nu'_{i'}\rangle \langle \nu'_{i'}| |\psi(t)\rangle \quad (54)$$

$$= \sum_{i=0}^{N_{\mathcal{H}}-1} |\nu_i\rangle \langle \nu_i| \sum_{n=0}^{\infty} \frac{(-i\delta)^n}{n!} \hat{H}^n \sum_{i'=0}^{N_{\mathcal{H}}-1} |\nu'_{i'}\rangle \langle \nu'_{i'}| |\psi(t)\rangle \quad (55)$$

$$= V_{N_{\mathcal{H}}}^\dagger \sum_{n=0}^{\infty} \frac{(-i\delta)^n}{n!} V_{N_{\mathcal{H}}} \hat{H}^n V_{N_{\mathcal{H}}}^\dagger V_{N_{\mathcal{H}}} |\psi(t)\rangle \quad (56)$$

$$\approx V_N^\dagger \sum_{n=0}^{\infty} \frac{(-i\delta)^n}{n!} V_N \hat{H}^n V_N^\dagger V_N |\psi(t)\rangle = V_N^\dagger e^{-i\delta T_N} V_N |\psi(t)\rangle, \quad (57)$$

with $(T_N)_{i,i'} := \langle \nu_i | \hat{H} | \nu_{i'} \rangle$ denoting the Krylov space representation of \hat{H} . Note that the approximation was introduced in Eq. (57), given that in general $N \ll N_{\mathcal{H}}$. Thus, by comparing Eq. (56) and Eq. (57), it becomes evident that the error introduced in the Taylor expansion is of the order of $\mathcal{O}(\delta^n/n!)$. It can thus be concluded that even a small number of iterations can result in a very small error. This is equivalent to the statement that due to the unique structure of the Krylov space $V_N^\dagger T_N^n V_N |\psi(t)\rangle$ will converge rapidly to $\hat{H}^n |\psi(t)\rangle$.

In the following, we can exploit the special property that T_N is tridiagonal, i.e. $(T_N)_{i,i'} = 0$ if $|i - i'| > 1$, in exact arithmetic to further simplify the evaluation of \hat{H} . While this is only strictly applicable in the context of exact arithmetic, enforcing this property will serve to enhance stability and numerical accuracy. By employing this property, it becomes evident that $V_N |\psi(t)\rangle$ in Eq. (57) can be written as

$$V_N |\psi(t)\rangle = || |\psi(t)\rangle || e_N^1, \quad (58)$$

as the first (normalized) Krylov vector $|\psi(t)\rangle$ is by construction orthogonal to all other Krylov vectors. In this context, e_N^1 represents an N -dimensional unit vector. Moreover, as T_N is merely $N \times N$ in size, it can be efficiently exponentiated through the utilisation of standard diagonalization algorithms. Making use of $T_N = Q_N^\dagger D_N Q_N$ results in

$$e^{-i\delta T_N} = Q_N^\dagger e^{-i\delta D_N} Q_N. \quad (59)$$

In this context, the notation D_N is used to denote the diagonal matrix that contains the eigenvalues of the matrix T_N . The matrix Q_N is used to represent a matrix that contains the respective left eigenvectors as rows. Upon inserting Eq. (58) and Eq. (59) into Eq. (57), we obtain the final equation

$$|\psi_N(t + \delta)\rangle = || |\psi(t)\rangle || V_N^\dagger Q_N^\dagger e^{-i\delta D_N} Q_N e_N^1. \quad (60)$$

This can be rewritten by defining the coefficient vector $c_N := Q_N^\dagger e^{-i\delta D_N} Q_N e_N^1$, resulting in

$$|\psi_N(t + \delta)\rangle = || |\psi(t)\rangle || V_N^\dagger c_N. \quad (61)$$

It is evident that the time evolved state $|\psi_{N_H}(t + \delta)\rangle$ comprises a sum over the Krylov vectors.

2.4.2 Errors and Numerical Efficiency

A number of convergence criteria and error bounds have been established for the error produced in the Krylov step. However, the majority of convergence criteria are imprecise and dependent on a specific interpretation. Moreover, the majority of error bounds have been derived for exact arithmetic, and thus may not be applicable to MPS. Accordingly, we will present the most practical error bound for the Krylov step.

The most significant bound that has been validated through empirical observation is that the Krylov error is of order $\mathcal{O}(\delta^N)$ if $\sqrt{W\delta} \leq N$ [80]. The quantity W is defined as the spectral range and is of the same order as the system size. This provides a reliable method for tuning the error so that it is comparable in magnitude to the other errors produced during the calculations.

In addition to the Krylov error, the method employed with MPS also gives rise to the truncation error. As usual, this error can be tracked using the discarded weight, and is typically of a negligible magnitude.

In conclusion, it can be stated that both errors can be effectively controlled and are typically of a relatively small magnitude, thereby rendering the method highly accurate. Nevertheless, this is at the expense of a relatively large numerical effort: The application of the Hamiltonian \hat{H} to $|\psi\rangle$, followed by the fusion of the legs, gives rise to a cost of $\mathcal{O}(D^3 w^3 d)$. The subsequent process of orthogonalisation results in a cost of $\mathcal{O}(D^3)$, see Sec. 2.4.5.

2.4.3 Use in combination with MPS

Thus far, we have considered a general derivation of the global Krylov method. We will now provide a brief overview of the simplifications introduced by expressing the quantum state as an MPS and the Hamiltonian \hat{H} as an MPO. The primary benefit of utilising MPS is that it allows for the efficient calculation of the final entry of the Krylov matrix $(T_N)_{N-1, N-1} = \langle \nu_{N-1} | \hat{H} | \nu_{N-1} \rangle$. In exact arithmetic, the matrix vector product $\hat{H} | \nu_{N-1} \rangle$ would have to be computed. In contrast, the use of MPS eliminates the necessity for this computation, as $\langle \nu_{N-1} | \hat{H} | \nu_{N-1} \rangle$ corresponds to an expectation value, namely the energy of the last Krylov vector. As applying the Hamiltonian to the most recent Krylov vector significantly increases its bond dimension, omitting this step for the final Krylov vector signifies a considerable

speedup of the algorithm.

As previously stated in Sec. 2.4.2, the time-evolved state $|\psi_{N_H}(t + \delta)\rangle$ is obtained by summing over N Krylov vectors. Given that each Krylov vector corresponds to a complete MPS, the bond dimension is doubled when two Krylov vectors are added and must be truncated afterwards. A number of techniques exist for truncating the bond dimension, see Sec. 2.1.5. We have selected variational compression as it is the most appropriate method for our purposes.

2.4.4 Caveats: Loss of Orthogonality

A significant challenge associated with this algorithm is the loss of orthogonality of the Krylov vectors due to finite numerical precision. It is essential to recognise that ensuring the quality of the Krylov space is of the utmost importance in order to obtain accurate time evolution.

As previously stated, truncation is necessary when using MPS, thereby reinforcing the significance of these issues. It would be reasonable to assume that the use of a Gram-Schmidt-type procedure would be the optimal method for orthogonalising the vectors with respect to each other. However, this procedure results in the addition of multiple MPS (direct sum), necessitating further truncation to reduce the bond dimension. This ultimately leads to a paradoxical loss of orthogonality.

One potential solution to this issue is the use of a method known as 'variational orthogonalization' with respect to all previous Krylov vectors [95]. This can be understood as a variational compression of a state under the constraint that it should have zero overlap with all previous Krylov vectors. In the context of Lagrange multipliers, this can be expressed as a minimization of

$$\|\hat{H}|\nu_i\rangle - |\nu_{i+1}\rangle\|^2 + \sum_{i'} \beta_{i'} \langle \nu_{i+1} | \nu_{i'} \rangle \quad (62)$$

with respect to $|\nu_i\rangle$ and $\beta_{i'}$. By employing an iterative scheme proposed in [95], this can be solved in terms of a series of local 1s or 2s problems. It should be noted, however, that the enhanced convergence of the 2s scheme is accompanied by the necessity of truncation after each local step, which has the potential to destroy the orthogonality of Krylov vectors. It is therefore recommended that, in practice, a few sweeps be performed with a 2s scheme, followed by a single site scheme, in order to ensure orthogonality. It should be noted that orthogonalization may be over-constrained if the vector space at the first few sites is of a very limited size. In such instances, it is recommended that the constraints be introduced sweep by sweep. The orthogonalisation may be performed either during the application of the Hamiltonian to the state in the form of a variational MPO-MPS application, or subsequently. In the following we will explain the latter approach, as it has been demonstrated to be advantageous in the context of long-range interactions, such as those occurring on a cylinder.

2.4.5 Variational Orthogonalization

The objective of this method is to identify the MPS $|\phi\rangle$ representing a given state $|\psi\rangle$ in an optimal manner, while ensuring that the constraint $\langle\phi|\psi_k\rangle = 0$ for a set $\{|\psi_k\rangle\}$ is satisfied. The variational orthogonalization follows a similar pattern as the variational compression: (i) As initial state we choose $|\phi\rangle = |\psi\rangle$. (ii) Subsequently, we calculate overlaps between the states $\langle\phi|$ and $|\psi\rangle$, which we designate as LR , and overlaps between $\langle\phi|$ and $|\psi_k\rangle$, which we designate as \mathcal{LR} . It should be noted that the overlaps LR have already been encountered in Sec. 2.1.5 on variational compression. (iii) Subsequently, we sweep through the system and undertake replacements on s adjacent sites: Initially, replacements are made that are equivalent to variational compression, with the objective of reducing the bond dimension

$$A_l \cdots A_{l+s-1} = \sum_{\alpha_1 \cdots \alpha_{s+1}} [L_l]_{\gamma, \alpha_1} [B_l]_{\alpha_1, \alpha_2}^{\sigma_l} \cdots [B_{l+s-1}]_{\alpha_s, \alpha_{s+1}}^{\sigma_{l+s-1}} [R_{l+s}]_{\alpha_{s+1}, \beta}, \quad (63)$$

where A represents the MPS tensors of $|\phi\rangle$, while B denotes the tensors of $|\psi\rangle$. It should be noted that in this instance, either the 1s or 2s scheme is employed, i.e. $s = 1$ or $s = 2$.

Subsequently, a projector \hat{P}_l in the space orthogonal to $|\psi_k\rangle$ is applied, resulting in

$$A_l \cdots A_{l+s-1} = \hat{P}_l A_l \cdots A_{l+s-1}. \quad (64)$$

The following derivation outlines the construction of the projector. We begin by considering the single overlap $\langle\phi|\psi_k\rangle = 0$. Given that this is a linear form in all tensors of $|\phi\rangle$, we can reformulate the condition that $|\phi\rangle$ is orthogonal to $|\psi_k\rangle$ for a given block of s tensors with all the other tensors held fixed as

$$\langle\phi|\psi_k\rangle = 0 \Rightarrow \left(\frac{\delta}{\delta A_l^\dagger \cdots A_{l+s-1}^\dagger} \langle\phi|\psi_k\rangle \right) A_l^\dagger \cdots A_{l+s-1}^\dagger = 0 \quad (65)$$

$$\equiv F_l^{\{k\}} A_l^\dagger \cdots A_{l+s-1}^\dagger = 0. \quad (66)$$

In this context, $F_l^{\{k\}}$ represents a tensor of rank $s + 2$, which has the same form as $A_l \cdots A_{l+s-1}$. Thus, we can express the projector \hat{P}_l in a manner inspired by the Gram-Schmidt procedure as

$$\hat{P}_l = \hat{1} - \sum_{k, k'} F_l^{\{k\}} [\mathcal{N}^{-1}]_{k, k'} F_l^{\{k'\} \dagger}, \quad (67)$$

where $[\mathcal{N}^{-1}]_{k, k'}$ is defined as the k, k' th element of the inverse of the Gram matrix \mathcal{N} , with

$$[\mathcal{N}]_{k, k'} = \text{Tr}(F_l^{\{k\} \dagger} F_l^{\{k'\}). \quad (68)$$

It should be noted that, due to the construction of $F_l^{\{k\}}$ the projector \hat{P}_l acts on a tensor of the shape $A_l \cdots A_{l+s-1}$ and returns a tensor of the same shape. Here we used the inverse of the Gram matrix to ensure that the projector is idempotent, i.e. $\hat{P}_l^2 = \hat{P}_l$.

To enhance the efficiency of this algorithm, an alternative approach could be to compute the eigenvectors of the inverse Gram matrix and express the $F_l^{\{k\}}$ with them. This would effectively transform the double sum in Eq. (67) into a single sum. However, determining the eigenvectors of the inverse Gram matrix may prove to be an ill-conditioned and singular problem. An alternative approach that is stable and is based on the same idea is to compute the so-called Moore-Penrose pseudoinverse [96] of the Gram matrix

$$[\mathcal{N}^+]_{k,k'} = \sum_{\mu=1}^{n_p} V_{k\mu} \frac{1}{\lambda_\mu} V_{k'\mu}^\dagger, \quad (69)$$

where V is the matrix containing the eigenvectors of \mathcal{N} as columns. Note that λ are defined as the n_p eigenvalues of \mathcal{N} , which are greater than $n\lambda_{max}\epsilon$. In this context, n represents the linear dimension of \mathcal{N} , while ϵ denotes the machine precision.

Finally, the use of the pseudoinverse allows us to obtain

$$G_l^{\{\mu\}} := \frac{1}{\sqrt{\lambda_\mu}} \sum_k V_{k\mu} F_l^{\{k\}} \quad (70)$$

$$\hat{P}_l = \hat{1} - \sum_{\mu} G_l^{\{\mu\}} G_l^{\{\mu\}\dagger}. \quad (71)$$

It is important to note that the process of finding $G_l^{\{\mu\}}$ is of the order of $\mathcal{O}(D^2)$, which is very efficient. Furthermore, it is also possible to efficiently compute the linear forms $F_l^{\{k\}}$ using the overlaps \mathcal{LR} as

$$F_l^{\{k\}} = \sum_{\alpha_1 \cdots \alpha_{s+1}} [\mathcal{L}_l^{\{k\}}]_{\gamma, \alpha_1} [B_l^{\{k\}}]_{\alpha_1, \alpha_2}^{\sigma_l} \cdots [B_{l+s-1}^{\{k\}}]_{\alpha_s, \alpha_{s+1}}^{\sigma_{l+s-1}} [\mathcal{R}_{l+s}^{\{k\}}]_{\alpha_{s+1}, \beta}, \quad (72)$$

where $B_l^{\{k\}}$ represent the MPS tensors of $|\psi_k\rangle$. Given the efficient iterative method for computing and updating $F_l^{\{k\}}$ during sweeping, it is straightforward to compute the projector \hat{P}_l and ensure orthogonality of the truncated MPS in a variational manner.

Note that in our computations we make use of a scheme that combines variational orthogonalization with CBE to enhance performance. It should be noted, however, that in this instance the object to be minimised by CBE differs from the one encountered in combination with TDVP, see Sec. 2.3.

2.5 Purification

This section is based on [12, 76–79, 86–88, 97]. There are a number of techniques that can be employed to simulate mixed states using MPS. These include a direct representation of the density matrix as an MPO, via minimally entangled typical thermal states (METTS), and purification. In the METTS approach, the sum over the eigenstates of the density matrix $\hat{\rho}$ is performed using a Monte Carlo scheme. In the case of only a few eigenstates with significant weight, this approach has been demonstrated to be effective [98]. However, when considering a full-rank thermal density matrix at a finite temperature, it is more advantageous to employ a purification scheme, which, in addition, permits calculations to be performed using the MPS formalism previously introduced. Accordingly, we will focus on this scheme in the remaining part of this discussion.

The fundamental concept of purification is to represent the density matrix $\hat{\rho}$ of an arbitrary mixed state in terms of a pure state $|\psi\rangle$. In order to achieve this, it is necessary to double the Hilbert space \mathcal{H} by introducing a so-called 'auxiliary' or 'ancilla' (a) space. The ancilla space may be interpreted as a heat bath coupled to the physical system in question. This doubling of the Hilbert space is done for every physical (p) state, resulting in a purified state

$$|\psi\rangle = \sum_{\alpha} |\alpha\rangle_a |\alpha\rangle_p \sqrt{\rho_{\alpha}} \in \mathcal{H}_a \otimes \mathcal{H}_p, \quad (73)$$

where $|\alpha\rangle_p$ represents the eigenstates of $\hat{\rho}_p$, while the corresponding eigenvalues are represented by ρ_{α} . In this context, the density matrix for a general mixed state $\hat{\rho}_p$ is defined in diagonal form as

$$\hat{\rho}_p = \sum_{\alpha} |\alpha\rangle_p \rho_{\alpha} \langle\alpha|_p. \quad (74)$$

It should be noted that the pure state can also be interpreted as a Schmidt decomposition on $\mathcal{H}_a \otimes \mathcal{H}_p$. Furthermore, it is essential to highlight that the operators act solely on the physical space, leaving the ancilla space unaffected. The purified state, see Eq. (73), can be represented using MPS in a manner analogous to MPO. However, in this case, the upper legs are living in the auxiliary space, see Fig. 6. This results in the formation of supersites, which are comprised of two legs living in local space: one in physical and the other in auxiliary space. As an alternative approach, the number of lattice sites can be doubled, which corresponds to a doubling of the Hilbert space. However, the supersite approach is more advantageous when utilising the CBE algorithm, as the local dimension increases up to d^2 . Moreover, the MPO implementation of the Hamiltonian must be adopted when the number of sites is doubled, as it is only permitted to act on the physical space. By tracing over the auxiliary space of $|\psi\rangle \langle\psi|$ one obtains the physical density matrix $\hat{\rho}_p$

$$\begin{aligned}\mathrm{Tr}_a |\psi\rangle \langle\psi| &= \sum_{\beta} \sum_{\alpha, \alpha'} \langle\beta|\alpha'\rangle_a \langle\alpha'\rangle_p \sqrt{\rho_{\alpha}} \sqrt{\rho'_{\alpha}} \langle\alpha|_p \langle\alpha|\beta\rangle_a \\ &= \sum_{\alpha} |\alpha\rangle_p \rho_{\alpha} \langle\alpha|_p = \hat{\rho}_p.\end{aligned}\quad (75)$$

Furthermore, the purification is supported by the observation that expectation values calculated using purified states correspond to expectation values of the respective mixed states

$$\langle\psi|\mathbb{1}_a \otimes \hat{O}_p|\psi\rangle = \sum_{\alpha, \alpha'} \sqrt{\rho_{\alpha}} \langle\alpha'|_p \langle\alpha'|_a \mathbb{1}_a \otimes \hat{O}_p |\alpha\rangle_a |\alpha\rangle_p \sqrt{\rho'_{\alpha}} \quad (76)$$

$$= \sum_{\alpha} \langle\alpha|_p \hat{O}_p |\alpha\rangle_p \rho_{\alpha} = \mathrm{Tr}_p \hat{\rho}_p \hat{O}_p = \langle\hat{O}_p\rangle. \quad (77)$$

In this derivation, we have assumed that $\hat{\rho}_p$ is normalised. Otherwise, the expectation value would have to be divided by the trace of $\hat{\rho}_p$, which is equal to the norm of the purified state

$$\langle\psi|\psi\rangle = \sum_{\alpha, \alpha'} \sqrt{\rho_{\alpha}} \langle\alpha'|_p \langle\alpha'|_a |\alpha\rangle_a |\alpha\rangle_p \sqrt{\rho'_{\alpha}} = \sum_{\alpha} \rho_{\alpha} = \mathrm{Tr}_p \hat{\rho}_p. \quad (78)$$

Thus far, our discussion has focused on the general case of an arbitrary mixed quantum state. We now turn to a system at finite temperature that is currently in equilibrium.

The equilibrium density matrix $\hat{\rho}_{\beta}$ is defined as

$$\hat{\rho}_{\beta} = e^{-\beta \hat{H}_p} = \sum_{\alpha} |\alpha\rangle_p e^{-\beta E_{\alpha}} \langle\alpha|_p, \quad (79)$$

where E_{α} denotes the eigenvalues of the Hamiltonian \hat{H}_p .

The norm is defined as the well-known partition function $Z(\beta)$, with

$$Z(\beta) = \mathrm{Tr}_p \hat{\rho}_p = \sum_{\alpha} e^{-\beta E_{\alpha}}. \quad (80)$$

Upon consideration of equations Eq. (73) and Eq. (79) it becomes evident that the purified version is defined as

$$|\psi_{\beta}\rangle = \sum_{\alpha} |\alpha\rangle_a |\alpha\rangle_p e^{-\beta \hat{H}_p/2} = \sum_{\alpha} |\alpha\rangle_a |\alpha\rangle_p e^{-\beta E_{\alpha}/2}. \quad (81)$$

It is also of practical importance to note that the infinite temperature purified state can be readily expressed in terms of a maximal auxiliary physical (max. aux-phys.)

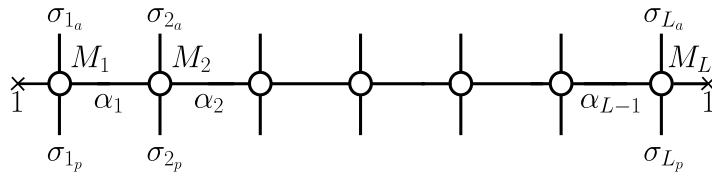


Figure 6: General purified quantum state, represented as MPS in a supersite shape. In this context, the index p denotes physical degrees of freedom, while a represents auxiliary degrees of freedom.

entangled state, which corresponds to a product state over locally max. aux-phys. entangled sites

$$|\psi_0\rangle = \sum_{\sigma} |\sigma\rangle_a |\sigma\rangle_p = \sum_{\sigma} |\sigma_1\rangle_a |\sigma_1\rangle_p \cdots |\sigma_L\rangle_a |\sigma_L\rangle_p = \prod_{l=1}^L \left(\sum_{\sigma_l} |\sigma_l\rangle_a |\sigma_l\rangle_p \right). \quad (82)$$

In this instance, σ denotes the local basis states, as is typically done. Furthermore, note that we considered a system featuring L sites. It is straightforward to see that the representation in terms of a product of locally max. aux-phys. entangled sites is valid, given that $\hat{\rho}_\beta$ factorizes over all sites in the case of infinite temperature. This results in a product state over combined aux-phys sites. In the context of a spin system, one typically selects 'opposite' quantum numbers for the ancilla in comparison to the physical site. Consequently, one can work in a system with a reduced dimension of the total Hilbert space $\mathcal{H}_a \otimes \mathcal{H}_p$. To illustrate, for a system with spin $1/2$, one typically chooses local spin singlets at infinite temperature, which sets the z -component of the total spin to zero.

Nevertheless, the question of how to derive $|\psi_\beta\rangle$ from $|\psi_0\rangle$ remains unanswered. In examining Eq. (75), it becomes evident that an imaginary time evolution must be performed on the infinite temperature purified state $|\psi_0\rangle$ in order to reduce the temperature. This can be seen by considering

$$\hat{\rho}_\beta = e^{-\beta\hat{H}_p} = e^{-\beta\hat{H}_p/2} \hat{\mathbb{1}} e^{-\beta\hat{H}_p/2}. \quad (83)$$

We now employ the fact that $\hat{\mathbb{1}} = \hat{\rho}_0$, where $\hat{\rho}_0$ represents the equilibrium density matrix at infinite temperature. This allows us to rewrite Eq. (83) as

$$\hat{\rho}_\beta = e^{-\beta\hat{H}_p/2} \text{Tr}_a |\psi_0\rangle \langle\psi_0| e^{-\beta\hat{H}_p/2} = \text{Tr}_a e^{-\beta\hat{H}_p/2} |\psi_0\rangle \langle\psi_0| e^{-\beta\hat{H}_p/2}. \quad (84)$$

In the final step, the trace over the auxiliary space has been pulled out, as the Hamiltonian only acts on the physical space. By making use of Eq. (75), this results in a final equation for the equilibrium purified state at finite temperature

$$|\psi_\beta\rangle = e^{-\beta\hat{H}_p/2} |\psi_0\rangle. \quad (85)$$

It is evident that Eq. (85) is equivalent to performing an imaginary time evolution up to the time $\tau = -i\beta/2$. Furthermore, it should be noted that when combining Eq. (78) and Eq. (80), the partition function $Z(\beta)$ can be readily obtained by observing the normalisation factors of $|\psi_\beta\rangle$ when lowering the temperature. This provides a straightforward approach to carrying out thermodynamic calculations.

2.5.1 Ancilla space backward time evolution

Although the purification is straightforward to implement and enables the use of pre-existing methods for time evolution within the MPS framework, the typical time scales that can be reached at finite temperature are considerably shorter than those at $T = 0$. This can be attributed to the growth of entanglement in the system. At $T = 0$, excitation of the ground state in a restricted region, will result in localised growth of entanglement around the excited region over the course of time evolution. In contrast, at $T > 0$ the entanglement typically increases homogeneously throughout the system. It is noteworthy that this phenomenon persists even in the context of time-evolution of a purified state in equilibrium. This phenomenon can be attributed to the non-unique nature of the purification, which renders the associated entanglement growth 'nonphysical'. It should be noted that any unitary operator \hat{U}_a acting on the ancilla space can be applied to the purified state without affecting the physical behaviour. It is therefore possible to attempt to identify an optimal representation of the auxiliaries that would result in a reduction of this non-physical growth of entanglement. It has been proposed that a backward evolution on ancilla space

$$\hat{U}_a(t) = e^{i\hat{H}_a t} \quad (86)$$

significantly reduces the entanglement buildup during time evolution. A pedagogical illustration of this behaviour has been presented in [87] for a Heisenberg chain. In the following, we will focus on the spin flip terms as they are more relevant to the dynamics. Let us consider a supersite in our system, which combines the auxiliary σ_a and physical σ_p degrees of freedom and is spanned by $\{|\uparrow\uparrow\rangle, |\uparrow\downarrow\rangle, |\downarrow\uparrow\rangle, |\downarrow\downarrow\rangle\}$. The system is initially set up using a typical choice of local aux-phys spin singlets, see Sec. 2.5. Now, we aim to observe the action of the Hamiltonian on two neighboring supersites separated by the pipe | symbol.

If the Hamiltonian $H_p \otimes \mathbb{1}$ is applied to these sites, the physical spins will flip due

to the action of the spin flip terms

$$\downarrow\uparrow | \uparrow\downarrow \xrightarrow{(1/2)(S^+ \otimes \mathbb{1}) \otimes (S^- \otimes \mathbb{1})} (1/2) \uparrow\uparrow | \downarrow\downarrow \quad (87)$$

$$\uparrow\downarrow | \downarrow\uparrow \xrightarrow{(1/2)(S^- \otimes \mathbb{1}) \otimes (S^+ \otimes \mathbb{1})} (1/2) \downarrow\downarrow | \uparrow\uparrow. \quad (88)$$

However, if we begin from the same state and apply the Hamiltonian $-\mathbb{1} \otimes H_a$, which features a negative sign, to the ancilla space, the same transition will occur, but with the opposite sign

$$\downarrow\uparrow | \uparrow\downarrow \xrightarrow{(-1/2)(\mathbb{1} \otimes S^-) \otimes (\mathbb{1} \otimes S^+)} (-1/2) \downarrow\downarrow | \uparrow\uparrow \quad (89)$$

$$\uparrow\downarrow | \downarrow\uparrow \xrightarrow{(-1/2)(\mathbb{1} \otimes S^+) \otimes (\mathbb{1} \otimes S^-)} (-1/2) \uparrow\uparrow | \downarrow\downarrow. \quad (90)$$

Consequently, the time evolution using both \hat{H}_p and \hat{H}_a , which is determined by $H_p \otimes \mathbb{1} - \mathbb{1} \otimes H_a$, reduces to a trivial calculation. In practice, the simultaneous backward time evolution in the ancilla and forward evolution of the system in physical space has been demonstrated to be an effective approach, see Fig. 7. It is noteworthy that this implementation is significantly more efficient than previous implementations [86] utilising backwards evolution on ancilla space in terms of the minimum bond dimension required.

2.5.2 Two-site disentangler

Given that the entanglement is already growing during the imaginary time evolution, it is necessary to find an alternative to the backward evolution on ancilla space that will enable us to reduce the entanglement during the imaginary time evolution. In a previous study, Hauschild [79] proposed an algorithm that attempts to compute \hat{U}_a such that $\hat{U}_a |\psi\rangle$ exhibits minimal entanglement. This can be understood as a 'disentangling' procedure. The algorithm employs a sequence of local disentangling operations to gradually construct a network that defines \hat{U}_a . The local two-site unitary \hat{U} is constructed in such a way that the action of it minimizes the entanglement of an effective two-site wavefunction $|\theta'\rangle$, with $|\theta'\rangle := \hat{U} |\theta\rangle$. Given that the von Neumann entropy is a non-linear function of the reduced density matrix, we decide to minimize the second Rényi entropy $S_2(\hat{U} |\theta\rangle)$, defined as

$$S_2(\hat{U} |\theta\rangle) = -\log \text{Tr}(\hat{\rho}_{L,L'}^2) = -\log(Z_2), \quad (91)$$

in order to derive the two-site unitary \hat{U} .

In this context, $\hat{\rho}_{L,L'} = \text{Tr}_{R,R'}(\hat{U} |\theta\rangle \langle\theta| \hat{U}^\dagger)$ represents the reduced density matrix of the left half of the two-site system and the subscripts L or R denote the left or right half of the two-site system, respectively. In order to minimize S_2 it is evident that this corresponds to maximizing Z_2 . One may attempt to resolve this non-linear problem by means of an iterative approach. As a first step in this iteration, one may select $\hat{U}_1 = \mathbb{1}$. Let us consider the case where we are in the m -th iteration. We may

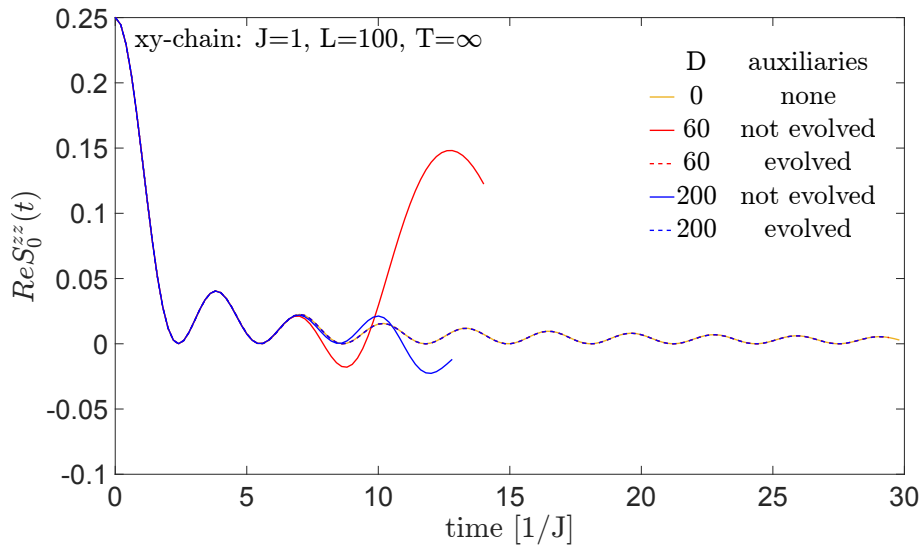


Figure 7: Benchmark to demonstrate the benefit of backward time evolution on ancilla space in combination with TDVP and CBE. We compute the infinite temperature longitudinal spin structure factor $S_n^{zz}(t)$ of a $L = 100$ site xy chain with spin coupling $J = 1$. $S_n^{zz}(t)$ is defined as follows: $S_n^{zz}(t) = \langle S_{L/2+n}^z(t) S_{L/2}^z \rangle$. We compare the exact result (solid brown/yellow line) with TDVP+CBE, both with (dashed blue and red lines) and without (solid blue and red lines) backward evolution of the auxiliary space. Despite the maximum bond dimension D being set to 60 and 200, the actual bond dimension required in TDVP+CBE combined with backward evolution on the auxiliary space was only 13.

now assume that \hat{U}_{m+1} is independent of the previous \hat{U}_m . Upon rewriting Z_2 in terms of \hat{U}_{m+1} , and the remaining environment $E_2(\hat{U}_m, \theta)$, the resulting expression reduces to

$$Z_2(\hat{U}_{m+1}, \hat{U}_m, \theta) = \text{Tr}(\hat{U}_{m+1} E_2(\hat{U}_m, \theta)). \quad (92)$$

From this, we can conclude that the optimal unitary \hat{U}_{m+1} maximizing Z_2 is obtained by performing an SVD on $E_2(\hat{U}_m, \theta)$, which results in

$$E_2(\hat{U}_m, \theta) = A\Lambda B^\dagger, \text{ with } \hat{U}_{m+1} = BA^\dagger, \quad (93)$$

where A and B^\dagger represent left and right isometries and Λ denotes the singular value spectrum of $E_2(\hat{U}_m, \theta)$. The rationale behind the definition of U_{m+1} , see Eq. (93), can be readily observed by inserting Eq. (93) into Eq. (92), resulting into

$$Z_2^{\text{updated}} = \text{Tr}(BA^\dagger A\Lambda B^\dagger) = \text{Tr}(\Lambda). \quad (94)$$

Consequently, the final \hat{U} , which is minimizing the entanglement, is obtained when the singular value spectrum of $E_2(\hat{U}_m, \theta)$ has reached convergence. For an illustration of the disentangling process, see Fig. 8.

It should be noted that this algorithm typically converges to a local minimum. In order to identify a global minimum, it is necessary to perform a number of computations with different initial disentanglers \hat{U}_1 and select the one featuring the smallest final entropy. It is also noteworthy that this algorithm only disentangles neighboring sites, thereby rendering it incapable of reducing the entanglement for sites situated at a greater distance. In order to achieve this, the use of swap gates may be employed. Furthermore, although the presented algorithm reduces the entanglement, it does not result in a reduction of the required bond dimension during computation due to the presence of a tail of small Schmidt values. Nevertheless, given that the numerical effort is strongly correlated with the amount of entanglement present in the system, it has proven to be a valuable tool.

2.6 MPO Implementation

In this section we explain in detail the MPO implementation procedure used for our numerical calculations. The procedure is inspired by finite state machines (FSMs) [99–103]. To facilitate understanding, we first explain the method at a more conceptual level. This is followed by a detailed presentation of how the technique can be combined with tensor networks.

2.6.1 Conceptual discription

For the sake of clarity, the procedure is presented below for the case of a two-dimensional Hubbard model on a square lattice

$$\hat{H}_{\text{Hubbard}} = U \sum_{\mathbf{i}} \hat{c}_{\mathbf{i}\uparrow}^\dagger \hat{c}_{\mathbf{i}\uparrow} \hat{c}_{\mathbf{i}\downarrow}^\dagger \hat{c}_{\mathbf{i}\downarrow} - t \sum_{\langle \mathbf{ij} \rangle, \sigma} (\hat{c}_{\mathbf{i},\sigma}^\dagger \hat{c}_{\mathbf{j},\sigma} + h.c.), \quad (95)$$

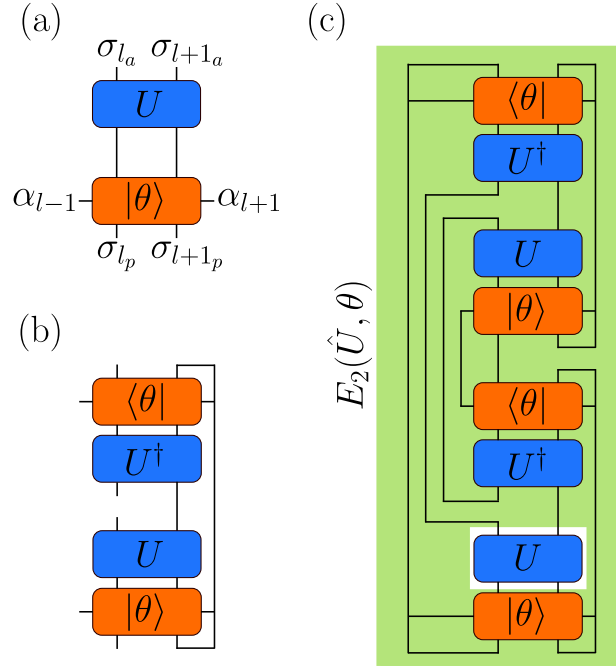


Figure 8: Illustration of the two-site disentangling algorithm. (a) Two-site wavefunction $|\theta\rangle$ to be disentangled by \hat{U} . (b) Tensor network diagram representing the reduced density matrix $\hat{\rho}_{L,L'} = \text{Tr}_{R,R'}(\hat{U}|\theta\rangle\langle\theta|\hat{U}^\dagger)$. (c) Tensor network diagram of $Z_2(\hat{U}, \theta) = \text{Tr}(\hat{\rho}_{L,L'}^2)$. The green area indicates the effective environment $E_2(\hat{U}_m, \theta)$, which is defined by $Z_2(\hat{U}, \theta) = \text{Tr}(\hat{U}E_2(\hat{U}, \theta))$.

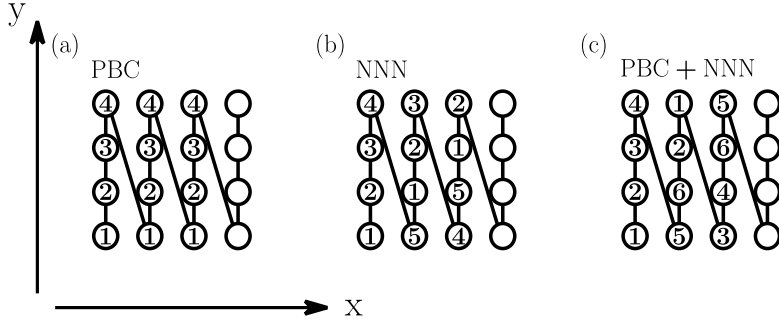


Figure 9: Illustration of the channels/states required to generate non-local terms. The line represents the MPS chain that we run through our system. The channel shown at a given site corresponds to the channel into which the first non-trivial character located at that site transitions in order to generate valid words. (a-c) Different scenarios with additional features are shown. Note that in all scenarios the Hamiltonian has NN interactions. (a) 2D square lattice with periodic boundary condition (PBC) in y-direction, corresponding to a cylinder. Note that the case without PBC would lead to the same states. (b) 2D square lattice with next nearest neighbour (NNN) interaction. (c) 2D square lattice with both PBC in the y-direction and NNN. This corresponds to a cylinder with NNN.

where \hat{c}^\dagger and \hat{c} represent the usual fermionic creation and destruction operators. To illustrate, running an MPS through a 4 x 4 lattice, see Fig. 9, will result in terms such as

$$\begin{aligned}
\hat{H} = & (U\hat{c}_\uparrow^\dagger\hat{c}_\uparrow\hat{c}_\downarrow^\dagger\hat{c}_\downarrow)_1 \otimes \mathbb{1}_2 \otimes \mathbb{1}_3 \cdots \mathbb{1}_{16} \\
& + \mathbb{1}_1 \otimes (U\hat{c}_\uparrow^\dagger\hat{c}_\uparrow\hat{c}_\downarrow^\dagger\hat{c}_\downarrow)_2 \otimes \mathbb{1}_3 \cdots \mathbb{1}_{16} \\
& \dots \\
& + (-t\hat{c}_\uparrow^\dagger\mathcal{P})_1 \otimes (\hat{c}_\uparrow)_2 \otimes \mathbb{1}_3 \cdots \mathbb{1}_{16} \\
& + \mathbb{1}_1 \otimes (-t\hat{c}_\uparrow^\dagger\mathcal{P})_2 \otimes (\hat{c}_\uparrow)_3 \otimes \cdots \mathbb{1}_{16} \\
& \dots \\
& + (-t\hat{c}_\uparrow^\dagger\mathcal{P})_1 \otimes \mathcal{P}_2 \otimes \mathcal{P}_3 \otimes \mathcal{P}_4 \otimes (\hat{c}_\uparrow)_5 \otimes \mathbb{1}_6 \cdots \mathbb{1}_{16} \\
& \dots,
\end{aligned}$$

where \mathcal{P} represents the parity operator and the subscript refers to the MPS site. In the following, the onsite interaction term will be abbreviated as the U term, and the hopping term will be abbreviated as the t term. The term 'character' will be used to refer to uniquely occurring sets of operators at a given site: $U\hat{c}_\uparrow^\dagger\hat{c}_\uparrow\hat{c}_\downarrow^\dagger\hat{c}_\downarrow \rightarrow U$, $-t\hat{c}_\uparrow^\dagger\mathcal{P} \rightarrow A$, $\hat{c}_\uparrow \rightarrow B$, $-t\hat{c}_\downarrow^\dagger\mathcal{P} \rightarrow C$, $\hat{c}_\downarrow \rightarrow D$, $t\hat{c}_\uparrow\mathcal{P} \rightarrow E$, $\hat{c}_\uparrow^\dagger \rightarrow F$, $t\hat{c}_\downarrow\mathcal{P} \rightarrow G$, $\hat{c}_\downarrow^\dagger \rightarrow H$, $\mathbb{1} \rightarrow I$, $\mathcal{P} \rightarrow P$. In accordance with this definition, the hopping terms on two neighboring MPS sites can be expressed as AB , CD , EF and GH . Furthermore, all

characters are often interpreted as an so-called alphabet Σ . Concatenating several elements of Σ results in the formation of a discrete sequence, referred to as a 'word' w . Consequently, each term in the Hamiltonian \hat{H} can be understood as a valid word. It follows that the set of all valid words can be used to express all terms in the Hamiltonian, thereby defining a so-called 'regular language',

$$\begin{aligned} \hat{H} = & UIIIIIIIIIIIII + IUIIIIIIIIIIIII + \dots \\ & IIIIIIIIIIIIIU + ABIIIIIIIIIIII + IABIIIIIIIIIIII + \dots \\ & APPPBIIIIIIIIII, \end{aligned}$$

where we have dropped the site subscript for readability. In order to provide an explicit example of how to generate a MPO from a regular language, we will write down the MPO in matrix format for a small system, which is relatively straightforward [12]. Running a MPS through a 3 x 3 lattice, this results in a local MPO tensor \hat{W}_l , located at site l within the chain, which can be expressed as

$$\hat{W}_l = \begin{pmatrix} I & 0 & 0 & 0 & 0 & 0 & 0 & 0 & 0 & 0 & 0 & 0 & 0 & 0 \\ A & 0 & 0 & 0 & 0 & 0 & 0 & 0 & 0 & 0 & 0 & 0 & 0 & 0 \\ 0 & P & 0 & 0 & 0 & 0 & 0 & 0 & 0 & 0 & 0 & 0 & 0 & 0 \\ 0 & 0 & P & 0 & 0 & 0 & 0 & 0 & 0 & 0 & 0 & 0 & 0 & 0 \\ C & 0 & 0 & 0 & 0 & 0 & 0 & 0 & 0 & 0 & 0 & 0 & 0 & 0 \\ 0 & 0 & 0 & 0 & P & 0 & 0 & 0 & 0 & 0 & 0 & 0 & 0 & 0 \\ 0 & 0 & 0 & 0 & 0 & P & 0 & 0 & 0 & 0 & 0 & 0 & 0 & 0 \\ E & 0 & 0 & 0 & 0 & 0 & 0 & 0 & 0 & 0 & 0 & 0 & 0 & 0 \\ 0 & 0 & 0 & 0 & 0 & 0 & 0 & P & 0 & 0 & 0 & 0 & 0 & 0 \\ 0 & 0 & 0 & 0 & 0 & 0 & 0 & 0 & P & 0 & 0 & 0 & 0 & 0 \\ G & 0 & 0 & 0 & 0 & 0 & 0 & 0 & 0 & 0 & 0 & 0 & 0 & 0 \\ 0 & 0 & 0 & 0 & 0 & 0 & 0 & 0 & 0 & 0 & P & 0 & 0 & 0 \\ 0 & 0 & 0 & 0 & 0 & 0 & 0 & 0 & 0 & 0 & 0 & P & 0 & 0 \\ U & B & 0 & B & D & 0 & D & F & 0 & F & H & 0 & H & I \end{pmatrix}. \quad (96)$$

It is readily apparent that the product of the operator-valued matrices \hat{W}_l , situated along the chain, will yield all terms in the Hamiltonian.

Next, we will continue with the 4 x 4 lattice and use the Finite State Machine (FSM) to create all valid terms in the Hamiltonian. In order to achieve this, we connect all sites that lead to a valid word. To illustrate, the word *APPPBIIIIIIIIII* corresponds to a horizontal hopping term between sites 1 and 5, which have to be connected via FSM in order to generate this word. For this purpose we use special 'states', which can be thought of as *channels*, so that each channel connects two (or more) sites. As is intuitively understandable, these channels live on the bonds between the sites that they connect. We will demonstrate in Sec. 2.6.2 that these channels live on the virtual bonds of the MPO. Consequently, the MPO bond dimension is directly correlated with the number of channels on a virtual bond. The idea is that there exist two 'global' channels, the so-called initial and final

states, which connect the trivial identities with each other, as well as the trivial part with the non-trivial part of each word. Considering the vertical hopping term $IIIIIIABIIIIIIII$, the identities positioned in front of the nontrivial hopping (AB) are connected by the initial channel, whereas the identities following the non-trivial hopping are connected by the final channel. Consistently, the nontrivial hopping (AB) is connected to the identities on the previous sites by the initial channel and to the subsequent sites by the final channel. Given that we are running an MPS/MPO chain through our system, the information flows from site 1 to site 2 to site 3 ... site 16. Therefore, the channels that live on bonds follow the same behavior. They flow in from the previous site, interact with the operator at the current site, and flow out to the next site. When the current channel interacts with a local operator, it can transition to a different channel. In the following, we will refer to a subscript as an incoming channel (from the previous site) and a superscript as an outgoing channel (to the next site). Consequently, we can represent our vertical hopping term $IIIIIIABIIIIIIII$ as

$$I_i^i I_i^i I_i^i I_i^i I_i^i (AB)_i^f I_f^f I_f^f I_f^f I_f^f I_f^f I_f^f, \quad (97)$$

where i represents initial and f the final channel. Note that, for now, we have neglected the channel that connects the A and B parts of the hopping term. We can observe that the non-trivial hopping AB changes the channel from initial to final. Having established how the trivial part of a word/term is coupled to the non-trivial part, we next explain how the local constituents within a non-trivial part are coupled to each other. To this end, we consider the horizontal hopping $IAPPPBIIIIIIIIII$ between sites 2 and 6, which we have already learned to interpret as $I_i^i (APPPB)_i^f I_f^f I_f^f I_f^f I_f^f I_f^f I_f^f I_f^f I_f^f$. In order to couple sites 2 and 6 as well as the parities in between, we define a special channel connecting all non-trivial sites of this hopping term. For the sake of convenience, we will refer to this channel as channel 'h' for hopping. Thus, the operator A takes in the initial channel and outputs the channel h, which is passed on by the other non-trivial sites as well. The final non-trivial character B takes the channel h and outputs the final channel to indicate that only trivial characters follow, i.e. $I_i^i A_i^h P_h^h P_h^h P_h^h B_h^f I_f^f I_f^f I_f^f I_f^f I_f^f I_f^f I_f^f I_f^f$. As we want to couple different sites in our square lattice, we require different channels in order to connect each pair of sites. To illustrate: $APPPBIIIIIIIIII$ (sites 1 and 5): channel 1, $IAPPPBIIIIIIIIII$ (sites 2 and 6): channel 2, $IIAPPPBIIIIIIIIII$ (sites 3 and 7): channel 3. Note that once $IIIIAPPPBIIIIIIIIII$ (site 5 and 9) is reached, we can reuse channel 1, since channel 1 is only required to exist between the sites 1 and 5 it originally aimed to couple. The same applies to the other channels. This results for a maximum of four channels required to couple the non-trivial constituents of every horizontal hopping term in \hat{H} , see Fig. 9.

Having gained an understanding of how to couple the horizontal hopping terms via channels/states, we next apply the same ideas to the vertical hopping terms and the onsite interaction terms. In the case of a vertical hopping term the already existing channels 1 to 4 can be used to connect the non-trivial constituents on neighbor-

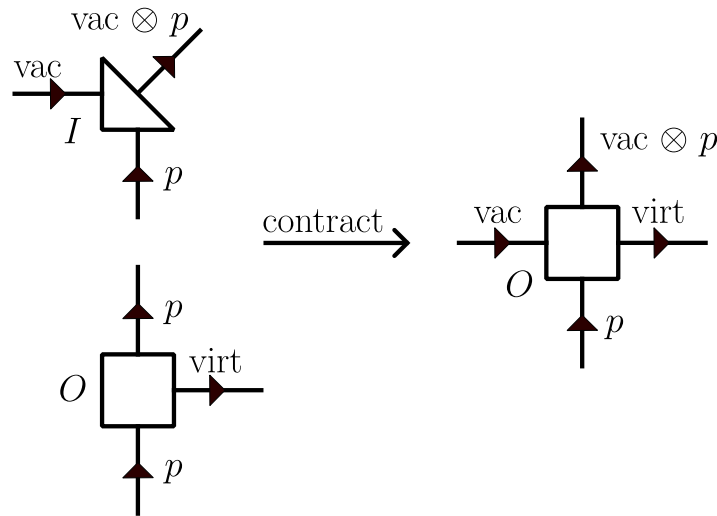


Figure 10: Process of adding a vacuum leg to an operator O . The final step (ii), which consists of contracting the identity operator I with the operator O , is displayed. In this context, the letter 'p' denotes the physical, while 'vac' or 'virt' denotes the respective vacuum or virtual legs.

activate the channel $m = 2$. The procedure is as follows: (i) Generate a two-leg identity operator I that lives on the state space of the leg that we want to expand. (ii) Iterate through the quantum number sectors and modify the reduced matrix element data of the identity operator I in each sector. We define the data in each sector as a $1 \times N$ matrix with only zeros. This is followed by setting the $(1, m)$ th data element equal to 1. (iii) Finally, we contract the identity operator I with the operator to be expanded. This results in an operator of dimension $2 \times 2 \times N$. The procedure can be seen in detail in Fig. 11.

As a consequence, two operators with equal quantum numbers and dimension along a leg that has been previously expanded, can only contract along that leg to a non-zero object, if that particular leg has been activated in the same channel m . From this perspective one should understand the statement that operators on two neighboring sites are coupled via a channel. Note that two operators with different quantum numbers on a leg will contract to an all-zero object, if contracted along that specific leg.

This allows for the straightforward assignment of channels for the 2D Hubbard model: Usually, it is advantageous to choose the vacuum leg as the leg carrying the initial and final channel. Therefore, they are expanded to dimension 2 and either activated in channel 1 (initial channel) or 2 (final channel). The non-trivial virtual legs of characters (A - H) are selected to carry the channels intended for hopping. In our example, they are expanded to dimension 4 to accommodate the maximum number of four channels required for hopping, and activated in a specific channel. As vacuum legs carry different quantum numbers compared to the non-trivial virtual

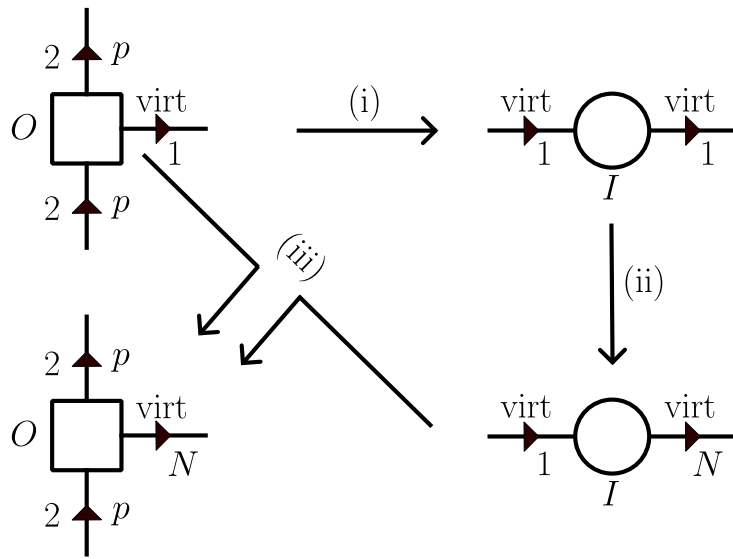


Figure 11: Procedure of expanding a virtual leg of a three-leg operator O of Hilbert space dimension $2 \times 2 \times 1$ by making use of identity operator I . The leg is expanded to allow for N channels. The same abbreviations employed in Fig. 10 are used to denote the respective legs. The number positioned adjacent to each leg correspond to its respective dimension. (i) Generate a two-leg identity operator I living on the virtual space. (ii) Modify the reduced matrix element data of the identity operator I . (iii) Contract the identity operator I with operator O .

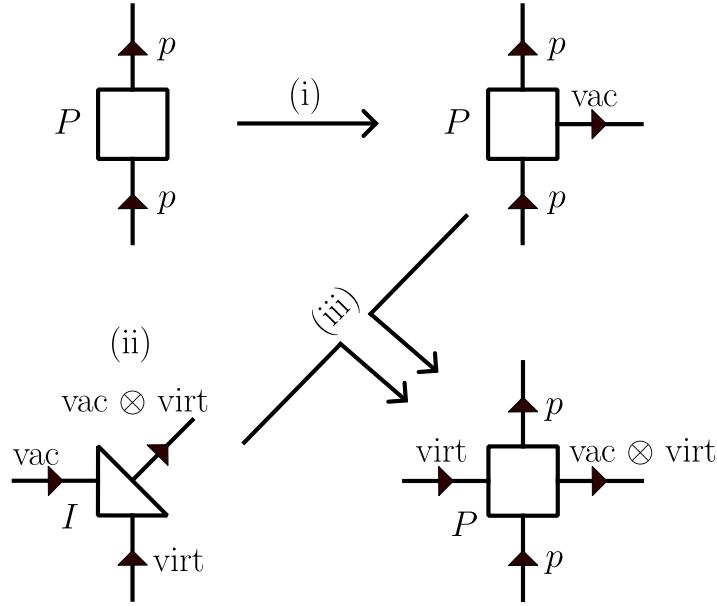


Figure 12: Procedure of expanding the parity P with two legs that carry the same quantum numbers as the non-trivial virtual legs of characters ($A-H$). The same abbreviations employed in Fig. 10 are used to denote the respective legs. (i) Add a vacuum leg to the parity P . (ii) Generate an identity operator I , mapping the space of the non-trivial virtual legs of characters ($A-H$) and the vacuum space onto their tensor product space. (iii) Contract the identity operator I and parity P .

legs, the hopping channels do not interfere with the initial/final channels.

It is also important to note that, in order to couple the parity operators of a horizontal hopping term to their respective creation/destruction operators via the hopping channels, see Sec. 2.6.1, we do not extend the parity P with vacuum legs. Instead, we use legs carrying the same quantum numbers as the non-trivial virtual legs of characters ($A-H$). This is achieved as follows: (i) Add a vacuum leg to the initially two-legged parity P . (ii) Build a three-leg identity operator I that maps the vacuum space and the space defined via the non-trivial virtual legs of characters ($A-H$) onto their tensor product space. (iii) Contract the parity P and the identity operator I along the vacuum leg. This effectively adds two legs corresponding to the non-trivial virtual legs of characters ($A-H$) to the parity P . The procedure is depicted in Fig. 12.

2.6.3 Summary

The procedure of implementing an MPO can be summarized as follows: (i) Expand all characters so that they take on a four-legged MPO shape, see Sec. 2.6.2. (ii)

Initialize the local MPO at each site with a four-legged identity, with both in and outgoing channels activated simultaneously in the initial and final states. As an exception, the identity on the first site is activated only in the initial channel, and the identity on the last site is activated only in the final channel. This marks the beginning and the end of each word. By initializing the MPO in this manner, the trivial part of all words of \hat{H} is already taken care of. (iii) Iterate all words of \hat{H} and place the non-trivial parts, activated in the correct channels, according to Sec. 2.6.1. When placing each character at a site, we add it to the already existing local MPO tensor. This process allows us to iteratively build up the entire MPO.

3 Results

This section presents the results of our study on magnetic polarons at finite temperature. We begin by discussing the details of the real-time dynamics, followed by an analysis of the spectral features.

3.1 Real time dynamics

In this section we want to shed light on the real-time dynamics of a single hole at different temperatures and coupling ratios. In the following we will also draw a comparison with the behaviour observed at $T = 0$. We will denote the time variable by τ , and plot it in units of either inverse tunneling $1/t$ or inverse exchange coupling $1/J$.

3.1.1 Background

Previous theoretical studies at $T = 0$ [18, 53, 54, 104] have shown conclusively that the dynamics of a hole follows a three stage process: (i) There is initial ballistic spreading of the hole with a velocity proportional to t , independent of J , up to time $1/t$. (ii) The magnetic polaron emerges as a meson, consisting of a holon and a spinon. (iii) Starting at times $1/J$, there is again ballistic spreading by the polaron with a velocity proportional to J and independent of t .

In order to verify the individual stages of the three stage process, one can define the Manhattan distance r [53]

$$r = \sum_x \sum_y (|x| + |y|) \cdot n^h(x, y), \quad (98)$$

where x and y denote positions within the lattice, and $n^h(x, y)$ the corresponding hole density. The origin, with $(x, y) = (0, 0)$, is defined as the initial hole location. By examining the time-dependence of r for $T > 0$, we study how far the hole is moving from its original position. Furthermore, this allows us to gain insight into the extent to which the polaron retains its characteristics at higher temperatures.

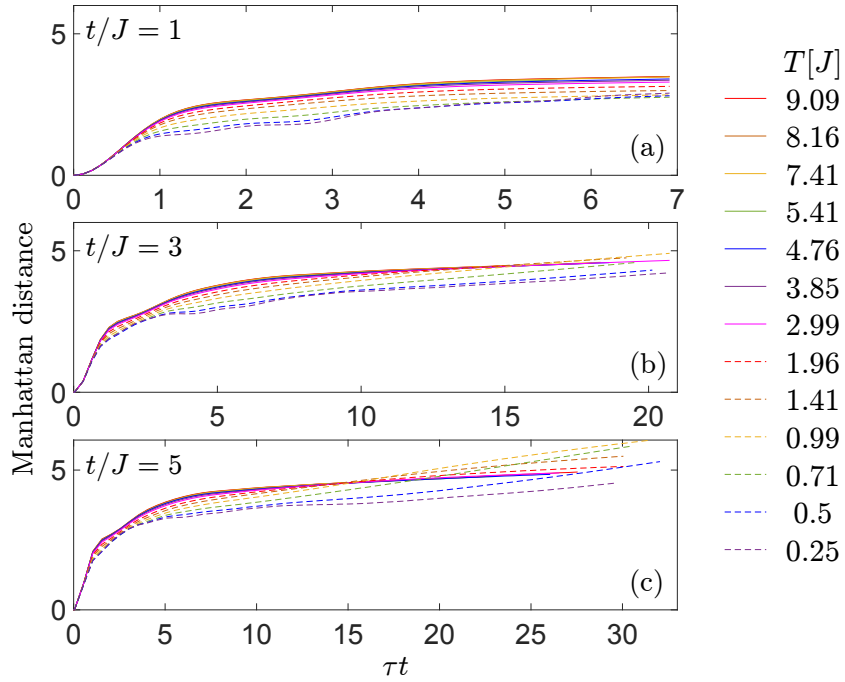


Figure 13: Dynamics of a hole at different temperatures in the two-dimensional t - J model on a square lattice. The calculations are performed for $t/J = 1, 3, 5$ on a cylinder with length $L_x = 18$ and width $L_y = 4$. The plots show the Manhattan distance as a function of time τ . At strong coupling, i.e. $t/J \gg 1$, and times larger $1/J$ we observe faster spreading at low temperatures (dashed lines) than at higher temperatures (solid lines).

3.1.2 Varying temperature

In Fig. 13, we compare r for multiple temperatures T , while keeping the coupling ratio t/J fixed. For all values of T and t/J , we observe the expected behaviour of an initial fast propagation of the hole, followed by slower propagation due to magnetic dressing. Note that this corresponds to a three stage process, similar to the three stages (i-iii) reported at $T = 0$, see Sec. 3.1.1. For an analysis of the extent to which the stages (i-iii) are still present at finite temperature, see Sec. 3.1.3.

Upon closer examination, we notice that only for $t/J = 1$, the distance $r(\tau)$ at fixed τ increases monotonically with temperature. For stronger coupling, $t/J > 1$, low-temperature values of r , see dashed lines, stay lower for times up to $1/J$, i.e. the stage of polaron emergence, but start to increase more quickly at times, $\tau \approx 3[1/J]$. As a result, $r(\tau)$ at fixed $\tau > 1/J$ is larger at intermediate temperatures than at large ones. This effect is more pronounced the higher t/J . In the parton picture, spin-spin-correlations are necessary for a finite string tension that constrains hole expansion and binds the holon to the spinon. Since the polaron is expected to propagate with a velocity proportional to the spin-coupling J , and spin-spin-correlations decrease with increasing temperature, see Fig. 19, implying a decrease in string tension, one could have conjectured that the slope of $r(\tau)$ vs. τ should monotonically increase with temperature for all times. Instead, at large τ the slope is seen to decrease with T . Thus, the T -dependence of the slope can not be attributed solely to a decrease in the effective spin coupling. We will further elaborate this point in the next subsection.

3.1.3 Varying the coupling ratio

In order to analyze the velocity of hole propagation, we compare the time evolution of the Manhattan distance $r(\tau)$ for three values of t/J while keeping the temperature fixed, see Fig. 14. The curves in Fig. 14(a-c) and Fig. 14(d-f) represent the same data, only for different scalings of the time axis, τt or τJ , focusing on the short-term (long-term) dynamics of the hole, respectively.

Fig. 14(a-c) reveals how the velocity initially does not depend on the spin-coupling J but only depends on hopping t , as can be seen by all curves lying on top of each other for shorter times. For all t/J values, an increase of temperature from $T = 0.25J$ to $T = 2.99J$ leads to an extension of the first stage of hole propagation, presumably due to a weakening of the spin correlations. This effect is most pronounced for $t/J = 1$. We interpret this as arising from a reduction in spin correlations, resulting in a reduction in string tension, with increasing temperature. Consequently, the time window within which the hole expansion only depends on hopping t increases. By taking a closer look at Fig. 14(d), featuring $T = 0.25J$, we notice that the three curves are approximately linear and parallel for larger times. Since the velocity can be estimated by dividing the Manhattan distance by time, and time is scaled in units of $1/J$, all three curves having the same slope verifies that the polaron velocity is proportional to J . However, upon increasing the temperature above $T = 0.25J$, the

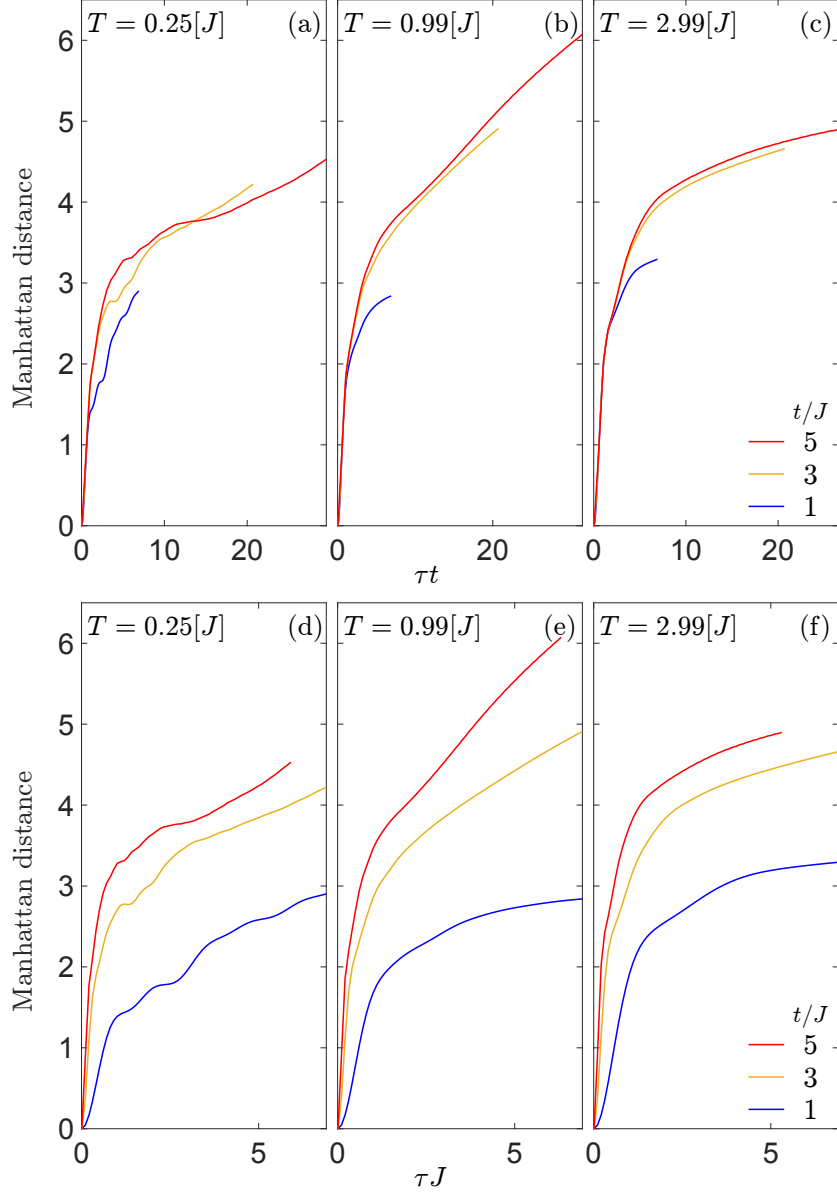


Figure 14: Analysis of the three stage process at finite temperature. (a-c) Manhattan distance is shown for three values of t/J at several temperatures as a function of time τ , plotted in units of $1/t$. (d-f) Analog to (a-c), but now plotted in units of $1/J$. The initial spreading still occurs with a velocity proportional to hopping t . For times beyond the emergence of the polaron we do only observe a simple proportionality of the expansion rate to the spin coupling J at low temperature $T = 0.25J$.

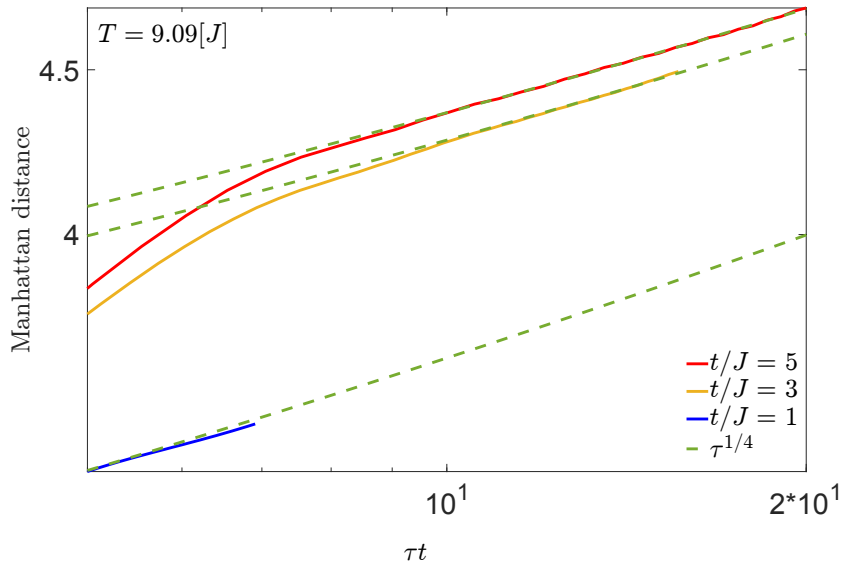


Figure 15: Analysis of the high temperature dynamics. Logarithmic plot of the Manhattan distance for different t/J as function of time. The data is plotted against a subdiffusive process (green dashed line), which has been shifted to coincide with the beginning of the respective long-term dynamics.

long time behaviour starts to differ. For $T = 0.99J$, see Fig. 14(e), the different graphs, no longer run parallel to each other at large times, pointing to a deviation from the behavior found for the polaron model at $T = 0$. For $T = 2.99J$, see 14(f), the non-parallel behaviour is less pronounced, but the three graphs are significantly more curved than for $T = 0.25J$.

Furthermore, the findings from Fig. 14(d-f) are reinforced from a different perspective. By scaling time in units of $1/t$, see Fig. 14(a-c), and increasing t/J , we effectively decrease J and expect a decrease of the velocity for longer times, at least for lower temperatures. This is visible in the $T = 0.25J$ -plot by the crossing of the curves for $t/J = 5$ (red) and $t/J = 3$ (yellow). For $T = 0.99J$ and $T = 2.99J$, this behaviour is absent, pointing again to a different behaviour of polarons at longer times.

3.1.4 Subdiffusion behavior at infinite temperature

By approximating the hole motion at infinite temperature as a quantum random walk on the Bethe lattice with a disorder potential [53], it was shown that the long-term propagation of the hole in the t - J_z model is subdiffusive when considering the case of infinite temperature and large J_z/t . Although our calculations are limited to a finite system size, which makes it difficult to observe diffusion processes, we have analyzed whether similar behavior can be observed for the more challenging t - J model.

In Fig. 15 we compare the intermediate to long-time Manhattan distance for our

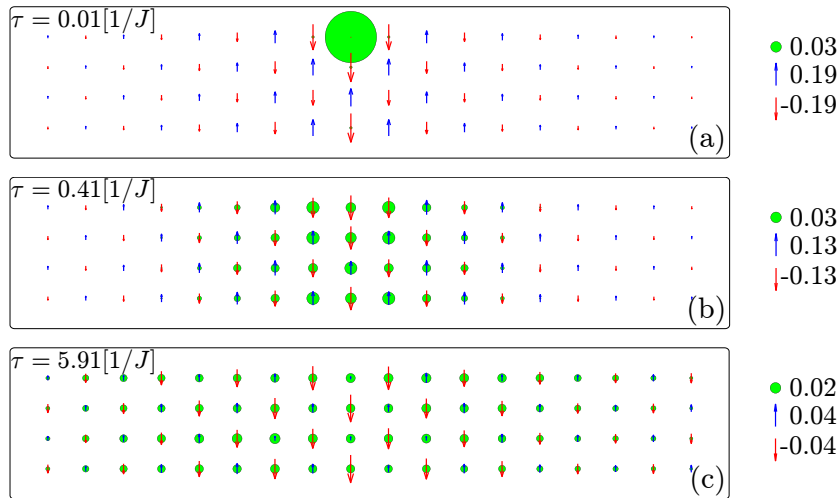


Figure 16: Hole density and spin across the entire lattice shown for several times at temperature $T = 0.25J$ for $t/J = 5$. The size of the green circles represents the strength of the hole density. Height and direction of the arrow correspond to absolute value and direction of spin.

highest temperature $T = 9.09J$ against the $\tau^{1/4}$ behaviour (dashed lines) expected for subdiffusive expansion. By scaling the time in units of $1/t$ and displaying the behaviour for different values of t/J , we effectively show how the spin coupling J affects the high temperature dynamics. For small spin couplings, i.e. $t/J \gg 1$ (red line), we find remarkably good agreement with the subdiffusion process displayed here. However, at $t/J = 1$ (blue line) the subdiffusive behaviour only holds for intermediate times and starts to break down for long times. This can also be understood in terms of a disorder potential on a Bethe lattice, which slows down the hole expansion. As a result of spin couplings, the movement of the hole from one site to another modifies the energy of the spin system, effectively creating the aforementioned disorder potential. Nevertheless, for the relatively large spin couplings J at $t/J \approx 1$ (blue line), the subdiffusive behavior is no longer observed. This phenomenon may be related to the spin flip terms present in the t - J model, which could amplify this effect in comparison to the t - J_z model. Consequently, this could result in the breakdown of subdiffusion for relatively large spin couplings J . It is also worth mentioning that the type of subdiffusion observed here is identical to the subdiffusion previously reported for the t - J_z model.

Furthermore, it is important to determine the temperature at which the subdiffusion behaviour ceases to exist. As the long-term behaviour for $T \geq 2.99$ remains essentially unaltered with temperature in the case of $t/J \gg 1$, see solid lines in Fig. 13, we conclude that for small spin couplings, i.e., $t/J \gg 1$, this subdiffusive behavior persists down to a temperature of $T \approx 2J$.

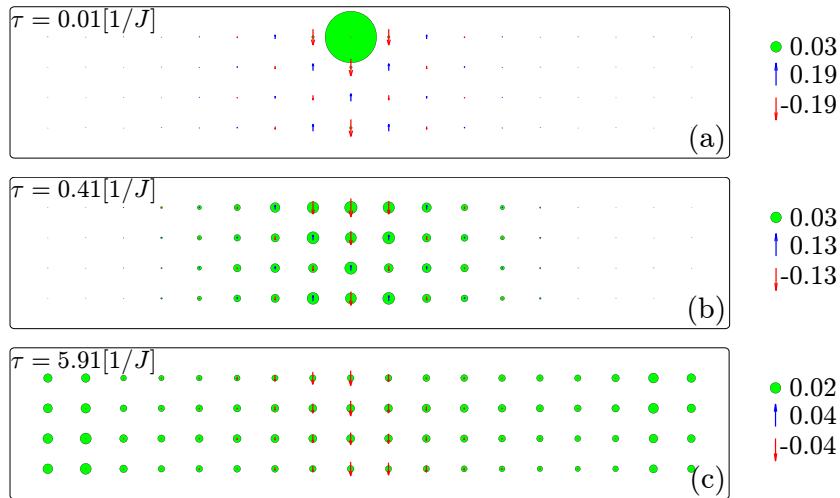


Figure 17: Hole density and spin across the entire lattice shown for several times at temperature $T = 0.99J$ for $t/J = 5$. The data is displayed in the same way as Fig. 16.

3.1.5 Hole density and spin across system

Thus far, our analysis has been limited to average distances. We now turn to site-resolved densities, which are directly accessible in quantum gas microscopes. In the following, we illustrate how both the hole density and spin evolve as a function of the lattice sites and as a function of time for a specific temperature $T = 0.25J$ with $t/J = 5$, see Fig. 16. At this point it is also important to mention that initially, an electron with spin down was removed from the equilibrium system, resulting in a total spin $S_z^{\text{tot}} \neq 0$.

In Fig. 16a we observe how the short-time symmetric spreading of the hole, starting at the initial hole position, results in spins being aligned in the same direction at sites adjacent to the initial hole position. This observation reflects that $S_z^{\text{tot}} \neq 0$. The initial hole position is located in the center of the cylinder and corresponds to the site with the largest hole density present at such short times. This indicates that the hole is still mainly located at the initial site.

At intermediate times, see Fig. 16b, the hole has already spread over one third of the length of the cylinder. In the process of spreading it has distorted the spin order around the initial hole position significantly more compared to Fig. 16a. Since displacing spins in an AFM background comes at an energy cost, this slows down the initial fast spreading of the hole at times $1/t$, which we observe here, and binds the holon to the spinon, both connected by the string of displaced spins. This corresponds to the emergence of a magnetic polaron.

Finally at long times, see Fig. 16c, we can see the reemergence of AFM correlations in the whole system and an almost uniform distribution of the hole density over the entire lattice, which indicates the imminent return of the system into equilibrium.

Fig. 17 presents analogous results at a higher temperature $T = 0.99[J]$. One observes

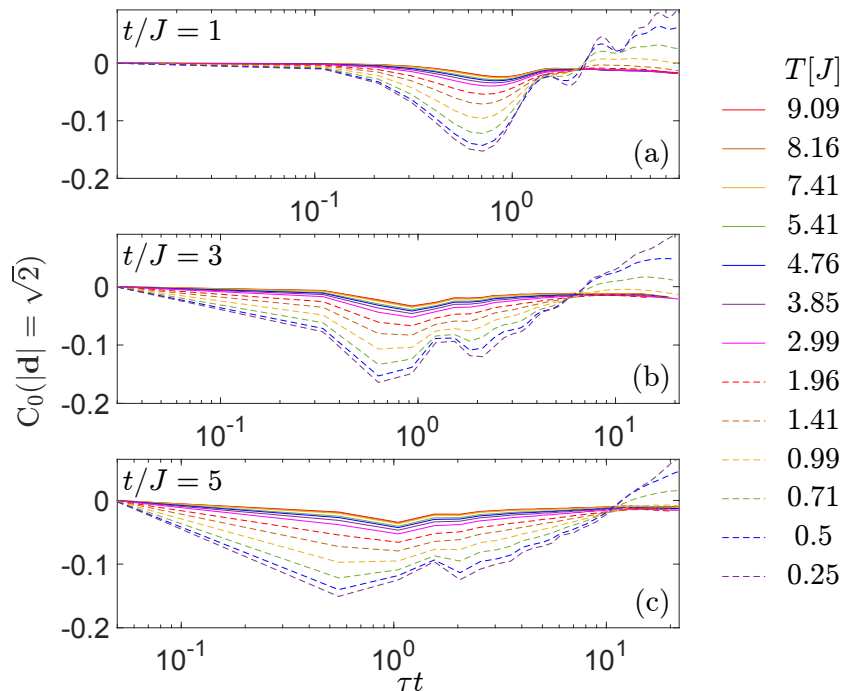


Figure 18: Sign-corrected next nearest neighbor spin correlations between the initial hole position and its diagonal neighbors as function of time. Data is displayed for several t/J at different temperatures.

a similar behaviour compared to Fig. 16, but the hole motion generally takes place faster and the average spin expectation value is reduced significantly. Nevertheless, the spatial heterogeneity of the hole density at long times indicates that the system has not yet reached a state of near-equilibrium, see Fig. 17c. This phenomenon may be attributed to either finite size effects or represents a distinctive feature of the doped system's dynamic. However at the same point in time one also observes a slight asymmetry in the spin data with respect to mirroring the data along the initial hole position. This presumably is due to accumulation of errors, which affect the rather small spins at such temperatures more severely. Furthermore we can see that no AFM correlations have built up close to the return to equilibrium, which is in line with Sec. 3.1.6 and Sec. 3.1.7.

3.1.6 Next nearest neighbor spin correlations

The process of polaron creation and subsequent polaron spreading, can also be analyzed by considering the evolution of spin correlations. In equilibrium, i.e. directly before we remove an electron from our system and study its dynamic, we can observe non negligible local AFM correlations for temperatures below $T = 0.99J$, see App. B.

To gain further insight on the evolution of spin correlations, we want to study sign-

corrected spin correlations, which are evaluated between sites \mathbf{r} and \mathbf{r}' and defined as

$$C_{\mathbf{r}}(\mathbf{d}) = (-1)^{d_x+d_y} 4(\langle S_{\mathbf{r}}^z S_{\mathbf{r}+\mathbf{d}}^z \rangle - \langle S_{\mathbf{r}}^z \rangle \langle S_{\mathbf{r}+\mathbf{d}}^z \rangle). \quad (99)$$

Here, \mathbf{d} is defined as the difference vector between respective sites \mathbf{r} and \mathbf{r}' and S^z is defined as the usual z -component of the spin operator \mathbf{S} . Note that as a consequence of this definition, positive correlation values correspond to AFM correlations.

We start by considering the corresponding next-nearest neighbor correlations $C_0(|\mathbf{d}| = \sqrt{2})$. Fig. 18 shows the sign-corrected next-nearest neighbor spin correlation (SCNNNC) as a function of time and relative to the initial hole position. This has been a common choice in experiment [105], facilitating comparisons with relative ease. The correlations are evaluated for different temperatures at three values of t/J .

We can observe for all values of t/J at all temperatures that the system is out of equilibrium during short and intermediate times, testified by the presence of negative correlation values, and only slowly approaches equilibrium for long times. For times up to $1/t$ the SCNNNC is negative and decreases even further in size. This is connected to the fast initial spreading of the hole with a velocity proportional to t . When the hole performs one hop, it places the neighboring spin on the "origin." As a result, the spin is situated in the "wrong" sublattice, leading to negative $d = \sqrt{2}$ spin correlations. During the phase of polaron emergence, which follows directly afterwards, the SCNNNC relaxes towards zero quickly and only slows down when the polaron is fully formed. At times larger $1/J$, when the polaron is moving as a whole, the SCNNNC continues to relax to equilibrium, but slower compared to the stage of polaron emergence. Given that the polaron is moving as a whole, the relaxation to equilibrium can also be understood as a consequence of spinon motion away from the origin.

Furthermore we can see that the negative correlations relax to equilibrium much faster for strong spin coupling, i.e. small t/J . This phenomenon can be attributed to the relaxation of spin correlation at the origin, which is a consequence of the motion of the spinon away from the origin. Given that spinon motion occurs on time scales of $1/J$, the findings presented on time scales of $1/t$, see Fig. 18, can be explained.

Since a finite string length of the polaron requires finite spin correlations [18, 51, 53], it is also of interest to determine the temperature up to which finite spin correlations are visible. This should indicate the transition to a region where no polarons emerge. We find an absence of spin correlations at all times for temperatures above $T = 2J$, with non-vanishing positive spin correlations only present at long times for temperatures smaller $T = 0.99J$. This temperature scale is in line with the temperature at which one would expect to see a return of AFM correlations due to a competition between temperature and spin coupling. In addition, the complete lack of spin correlations for temperatures above $T = 2J$ also suggests that magnetic polarons do not survive in that temperature range.

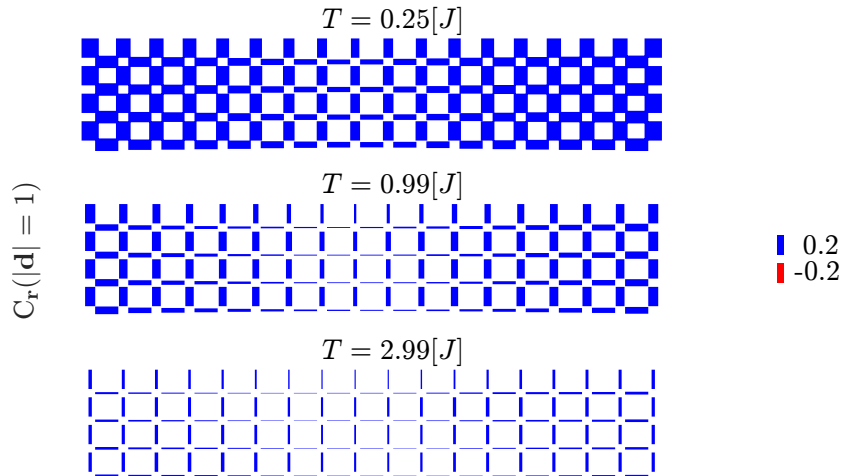


Figure 19: Sign-corrected nearest neighbor (SCNNC) spin correlations in the entire lattice for $t/J = 5$. Data is plotted at different temperatures at the maximum calculated time $\tau = 6/J$. The bars represent the SCNNC spin correlations connecting neighboring sites. The thickness and the color of the bars represents the absolute value and the sign of the spin correlation.

3.1.7 Nearest neighbor spin correlations

To further improve our intuitive understanding, we now build on the image created in Sec. 3.1.5 by discussing the distribution of spin correlations over the entire lattice as a function of temperature.

To this end, we take a closer look at the sign-corrected nearest neighbor (SCNNC) spin correlations, see Fig. 19. Here, we present the distribution of the spin correlations over the entire lattice for $t/J = 5$ at the maximal reached time $\tau = 6/J$. By examining the long-term correlations, we aim to determine whether we can identify features that are characteristic of a system close to equilibrium, such as a homogeneous spin correlation, or alternatively, whether we can observe features that must be explained due to the dynamics of the doped system.

Overall, we observe that the average strength of the spin correlation reduces with increasing temperature, as expected. Since these data only show non-vanishing spin correlations for temperatures below $T = 0.99J$, they support the observations of Sec. 3.1.6.

Furthermore, we see a fairly even distribution of spin correlation, only the spin correlations around the initial hole position have not yet reached equilibrium. This leads to the conclusion that the system is almost back in equilibrium at the end of the time evolution, in agreement with Sec. 3.1.5.

3.1.8 Spinon spreading

To conclude with the discussion of the real-time dynamics, we want to shed light on the spinon spreading. In order to achieve this, we define the spinon density as the normalized deviation of the SCNNC from its equilibrium value. It is crucial to acknowledge that this definition is only valid in the context of temperatures where polarons exist, see Sec. 3.2.3. Fig. 20 illustrates the Manhattan distance r_s of the spinon for varying values of t/J and temperatures. Overall, the data indicate that the spinon spreading also follows a three-stage process, similar to the spreading of the hole as a whole.

Within a single short time step, a pronounced increase in the spinon distance, r_s , is observed, with the greatest increase occurring at low temperatures. This can be attributed to the presence of AFM correlations in equilibrium at low temperatures. The removal of an electron and subsequent hopping of the hole for a short time step results in the emergence of ferromagnetic correlations adjacent to the initial hole position. This corresponds to a significant deviation from the equilibrium correlations, which is reflected in a steep increase in the spinon distance r_s .

Following the initial time step, the velocity of spinon spreading is observed to increase with temperature. This behaviour persists up to medium times and is especially pronounced in the case of $t/J > 1$. It is noteworthy that this behaviour is consistent with the behaviour of the hole as a whole, which also features an increase in spreading velocity with temperature in the case of $T < 2J$ and similar times, see Sec. 3.1.2.

At long times, $\tau > 1/J$, the velocity of spinon spreading is observed to be similar for different temperatures. However, the absolute spinon distance r_s reached at long times is slightly higher for lower temperatures. This is in contrast to the long-time spreading of the hole as a whole, see Sec. 3.1.2, which reaches further distances the higher the temperature in the case of $T < 2J$. It is likely that this discrepancy can be attributed to a reduction in the binding strength between the holon and the spinon as the temperature increases, which in turn permits a further propagation of the hole.

3.2 Spectral properties

Finally, we take a look at the spectral properties at finite temperature. Furthermore, we make a thorough comparison with the features observed at $T = 0$.

In the following the spectral function $S(\mathbf{k}, \omega)$ is defined as the Fourier transformation of the time-dependent correlation function $C_{\mathbf{i},\mathbf{j}}(t)$,

$$A(\mathbf{k}, t) = \sum_j e^{-i\mathbf{k}j} C_{\mathbf{0},j}(t) \quad (100)$$

$$A(\mathbf{k}, \omega) = \int_{-\infty}^{\infty} dt e^{-i\omega t} A(\mathbf{k}, t) \quad (101)$$

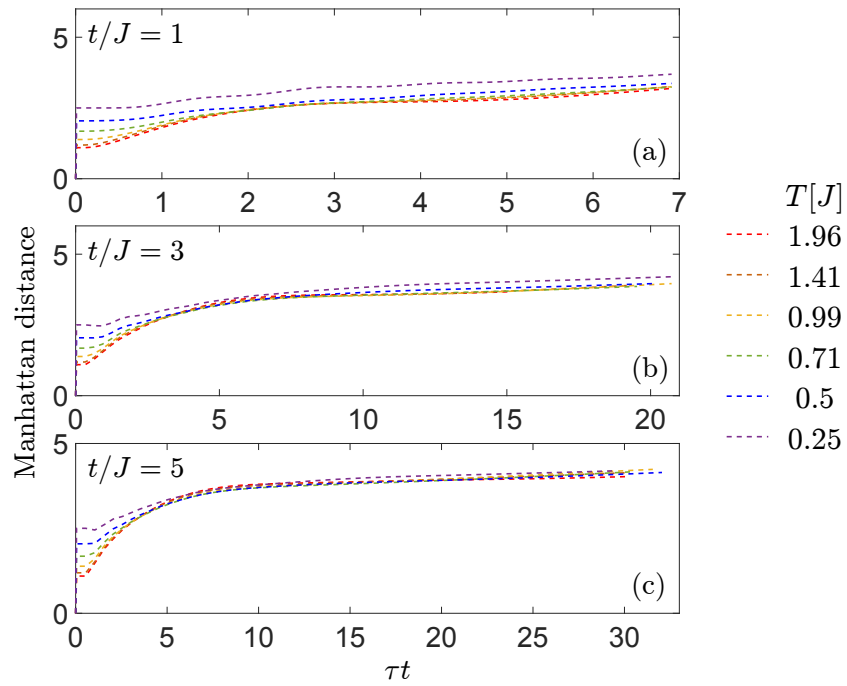


Figure 20: Manhattan distance of the spinon. The spinon density used here is defined as the normalized deviation of the SCNNC from its equilibrium value. The data is displayed for several t/J and different temperatures, up to which polarons are expected to exist.

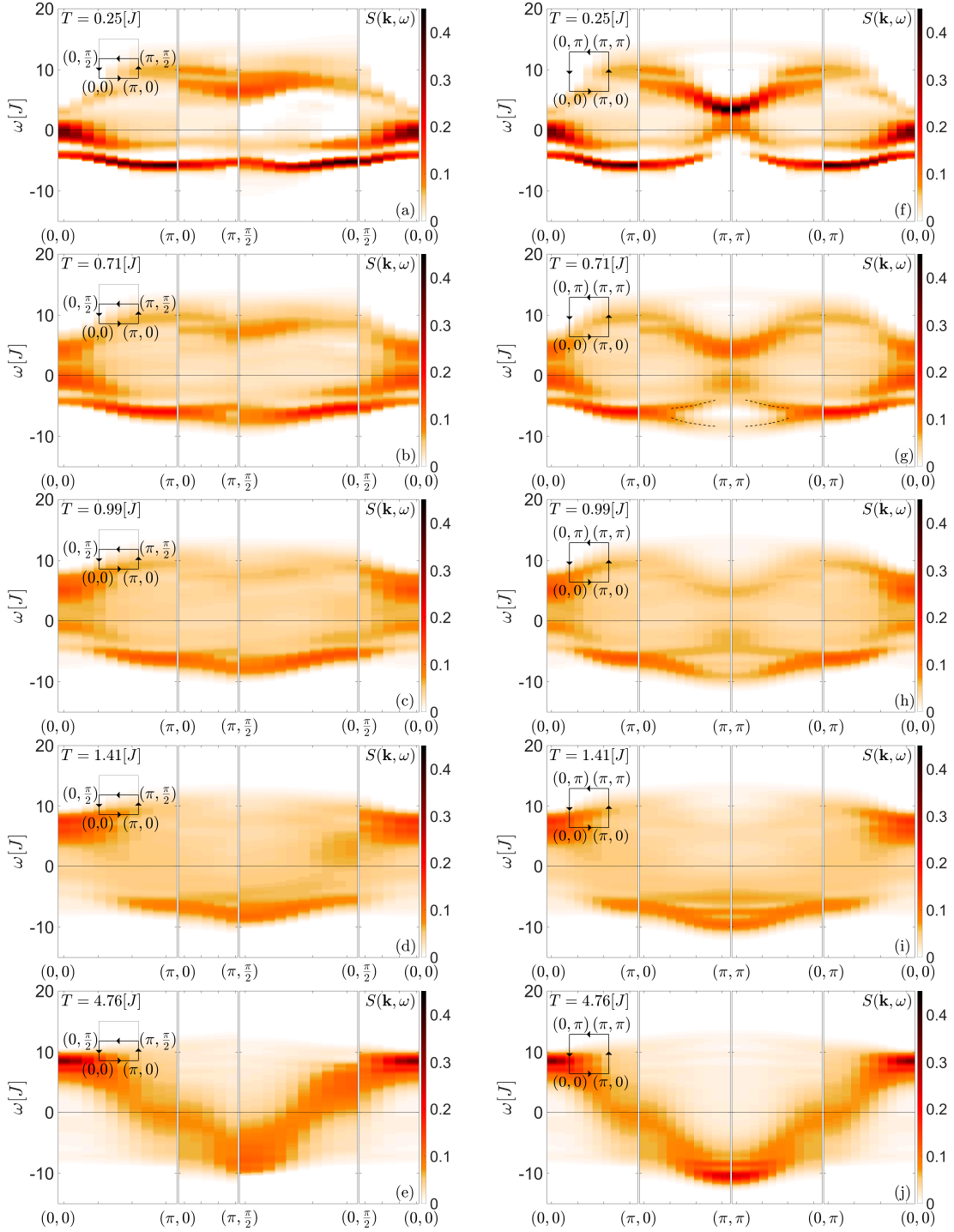


Figure 21: Spectral function for $t/J = 3$ going along two different paths in the Brillouin zone (BZ). Data is shown for several temperature values. The spectral function is obtained along cuts through the BZ. Note that the cuts in y -direction are symmetrized in order to allow for a high resolution in k_y . (a-e) Path goes through center of the BZ. (f-j) Path goes along the edge of BZ. The dashed lines in (g) mark the splitting of the ground state branch.

which finally results in

$$S(\mathbf{k}, \omega) = -\frac{1}{\pi} \Im A(\mathbf{k}, \omega). \quad (102)$$

Here $C_{\mathbf{i}, \mathbf{j}}(t)$ is defined in our purification formalism as

$$C_{\mathbf{i}, \mathbf{j}}(t) = -i \sum_{\sigma} \langle \psi_{\text{equil}}^{\text{puri}} | e^{i\hat{H}t} \hat{c}_{\mathbf{j}, \sigma}^{\dagger} e^{-i\hat{H}t} \hat{c}_{\mathbf{i}, \sigma} | \psi_{\text{equil}}^{\text{puri}} \rangle, \quad (103)$$

where \mathbf{i} and \mathbf{j} stand for the lattice sites for which the correlation function is to be calculated and \hat{c} (\hat{c}^{\dagger}) are the usual destruction (creation) operators. Here the sum runs over spin and $|\psi_{\text{equil}}^{\text{puri}}\rangle$ is the finite temperature purified state of the system in equilibrium.

In this context, the quasiparticle residue $Z(\mathbf{k})$ is defined as the frequency integral over the respective peak [54]

$$Z(\mathbf{k}) = \int_{\omega_-}^{\omega_+} d\omega S(\mathbf{k}, \omega). \quad (104)$$

It should be noted that, in the context of the geometric string theory picture, $Z(\mathbf{k})$ is proportional to the probability for a string of length zero [18].

3.2.1 Background

In the past, various semi-analytical and numerical methods have been used to study the spectral properties of a single hole in the 2D t - J model at $T = 0$. In the strong coupling regime, i.e. $t/J > 1$, the following low energy properties have been established [54], with energies not exceeding $2t$ above the one-hole ground state:

(i) At the lowest energies, $S(\mathbf{k}, \omega)$ exhibits a quasiparticle peak belonging to the magnetic polaron. The width is of the order of J , and the dispersion relation exhibits a minimum at the nodal point $(\pi/2, \pi/2)$ as well as low-energy states along the edge of the magnetic Brillouin zone.

(ii) The quasiparticle residue $Z(\pi/2, \pi/2)$ at the dispersion minimum at the nodal point depends strongly on t/J .

(iii) Above the magnetic polaron ground state a second peak has been observed at excitation energies $\Delta E < t$.

(iv) The first excitation peak can be observed for all momenta, as long as the ground state spectral weight is nonzero. Furthermore, it has been shown that the dispersion relation of the first excitation peak is qualitatively identical to that of the ground state. In the geometric string theory picture the first excited peak can be understood as a vibrational excitation of the polaron, featuring a energy scaling with the ratio of t/J [18].

(v) Around $\mathbf{k} = (\pi, \pi)$ the spectral function is suppressed for energies up to $\mathcal{O}(2t)$ above the ground state. This has been explained as a consequence of spinon statistics. Beyond that energy range, one finds a pronounced high energy feature.

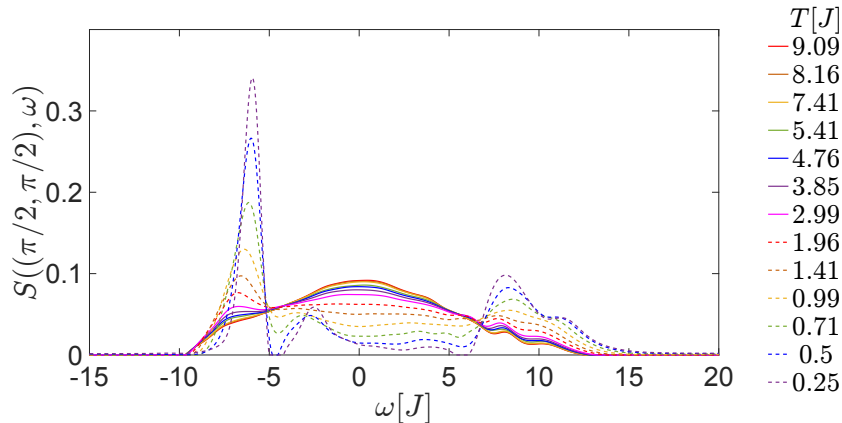


Figure 22: Spectral function for $t/J = 3$ evaluated at $\mathbf{k} = (\pi/2, \pi/2)$. This corresponds to a vertical cut through Fig. 21 at the point $\mathbf{k} = (\pi/2, \pi/2)$.

3.2.2 General observations at finite temperature

In order to extend our knowledge of the spectral properties of single holes and to test to what extent the properties (i-v) are present at finite temperature, we have calculated the spectral function at finite temperature, see Fig. 21. Here we calculated the spectral function $S(\mathbf{k}, \omega)$ for $t/J = 3$.

It is also worth mentioning that one needs to perform an additional forwards time-evolution on the equilibrium purified state $e^{-i\hat{H}t} |\psi_{\text{equil}}^{\text{puri}}\rangle$, see Eq. (103), besides our usual time-evolution describing the hole dynamics in order to calculate the overlap in Eq. (103). In order to extend the time window that we can use, we employed linear prediction [106] and multiplied the correlation function with a Gaussian envelope prior to Fourier transformation [107].

Note that the chosen value of $t/J = 3$, which is a typical value for high- T_c cuprates, lies within the strong coupling regime, but outside of the region where the Nagaoka effect is relevant [108]. Results for different values of t/J , which are still positioned in that regime, behave qualitatively similar, see App. A.

Beginning with some general observations, we find that at our lowest temperature $T = 0.25J$, spectral functions are qualitatively identical to $T = 0$ results, see [54]. Therefore if we compare with features (i-v), see Sec. 3.2.1, we find that all properties (i-v) are present for this low temperature. Further increasing temperature up to $T = 0.99J$, the spectral function looks qualitatively similar to the result at $T = 0$, but featuring some important differences, see Sec. 3.2.4, 3.2.5, 3.2.6. Above this temperature, the spectrum begins to deform more and more into a single band structure whose behavior is almost quadratic.

Next we look in more detail at some of the discussed features and examine whether they persist upon increasing temperature:

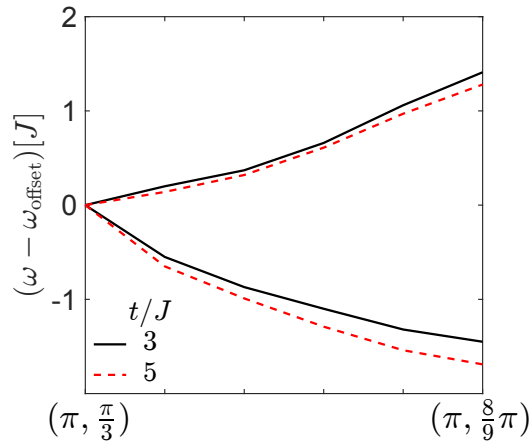


Figure 23: Peak locations of the two emerging branches in the spectral function, see dashed lines in 21(g), present at $T = 0.71J$ for $t/J = 3, 5$. The peak locations have been extracted for the vertical cut $(\pi, 0) \rightarrow (\pi, \pi)$. To facilitate comparison between the curves for different t/J , the peak locations have been shifted by an offset term $\omega_{\text{offset}}[J]$.

3.2.3 Temperature resistance of polarons

In order to test the validity of the polaron picture at finite temperature, we study the temperature dependence of polaron peaks, i.e. features (i),(iii): To this end, we evaluate the spectral function $S(\mathbf{k}, \omega)$ at a specific point in the BZ, see Fig. 22. We can resolve both the ground and first excited state of the magnetic polaron up to $T \approx 0.99J$. This demonstrates that polarons are relatively stable with respect to temperature and confirms the validity of the polaron picture even at intermediate temperature. Note that this is also consistent with the temperatures up to which non-negligible AFM correlations are present, see Sec. 3.1.6 and App. B, which is easy to understand due to the necessity of spin correlations for the existence of a finite string tension.

3.2.4 Dispersion relations of ground and first excited polaron states

Even though we have shown in Sec. 3.2.3 that polarons exist up to relatively high temperatures, it is also of interest to what extent the respective dispersion relations change with temperature, i.e. testing feature (iv): We observe that outside of the area around (π, π) , which shows some very interesting behavior at finite temperature (see 3.2.5), the dispersion relations of the first excitation peak and the polaron ground state remain qualitatively identical and basically unchanged with temperature as long as polarons are present, which includes temperatures up to $T \approx 0.99J$.

3.2.5 Suppression of the spectral weight around $\mathbf{k} = (\pi, \pi)$

In analogy with the $T = 0$ results, we also observe a suppression of the spectral weight around $\mathbf{k} = (\pi, \pi)$ for temperatures smaller $T = 0.5J$. This is accompanied by a high energy feature above that energy gap, which is also observed for $T = 0$. Above that temperature threshold, the ground state branch splits up into two new branches around $\mathbf{k} = (\pi, \pi)$ and closes that excitation gap, see dashed lines in Fig. 21(g). At the same time, we observe that the high-energy feature loses prominence, which suggests that these two phenomena are connected. It should be noted that the splitting of the ground state branch is absent in the case of $t/J = 1$, see App. A. In order to assess the nature of the two branches, we extracted the peak positions for $t/J = 3, 5$ and plotted them as function of $\omega[J]$, see Fig. 23. We observe that the upper branches remain almost independent of t/J , whereas the lower branch shows a significant alteration with t/J . This indicates that the two emerging branches are each either $\mathcal{O}(t)$ or $\mathcal{O}(J)$, suggesting that they indicate a spin-charge separation, with the peak located at $\mathcal{O}(J)$ corresponding to a spinon and the one located at $\mathcal{O}(t)$ to a chargon. Nevertheless, to confirm that the two branches are indeed of $\mathcal{O}(t)$ or $\mathcal{O}(J)$, further calculations at even higher values of t/J would be necessary, which would entail a significantly greater numerical effort.

The emergence of the two branches can be understood in the context of a mean-field parton theory as follows: In the case of $T = 0$, the suppression of the spectral weight at $\mathbf{k} = (\pi, \pi)$ was explained as a consequence of the Fermi-Dirac distribution of spinons, which leads to a sharp step in the spinon quasiparticle weight $Z_s^{MF}(k)$ [54]

$$Z_s^{MF}(k) = \begin{cases} 2, & |k| \leq \pi/2 \\ 0, & \text{else} \end{cases}, \quad (105)$$

which effectively suppresses the quasiparticle weight of the polaron in a region around (π, π) . At finite temperature, this sharp step becomes smooth, resulting in a decreasing spinon contribution to the quasiparticle weight as (π, π) is approached and ultimately leading to the quasiparticle weight reaching zero. As the quasiparticle weight approaches zero, the probability of a finite string length is reduced, which ultimately results in the decoupling of holon and spinon. This can be seen well at $T = 0.71[J]$ in Fig. 21 when approaching (π, π) in the ground state branch of the polaron. Note that this agrees with the deconfinement temperature $T \approx 0.65[J_z]$ reported for the t - J_z model [109].

3.2.6 Analysis of behavior around $\mathbf{k} = (0, 0)$

Previous results at $T = 0$ revealed in addition to the suppression of spectral weight around (π, π) , also a considerably weaker suppression of spectral weight around $(0, 0)$. The suppression is less severe compared to (π, π) and spectral weight starts to increase already slightly above the ground state peak. A prominent high energy feature is also missing compared to (π, π) . This suggested that different mechanisms are responsible for the behavior at (π, π) and $(0, 0)$.

We find that this suppression around $(0,0)$ gets more pronounced with increasing temperature, such that when the temperature is high enough that the gap at (π, π) is closed, see Fig. 21(g) at $T = 0.71J$ and Sec. 3.2.5, the ground state peak at $(0,0)$ is almost fully suppressed and a wide energy window with very low spectral weight has opened above the ground state energy. In contrast to the conclusion reached at $T = 0$, the observed correlation between the behaviour at $(0,0)$ and (π, π) suggests a connection between the two, which may be attributed to a common underlying mechanism.

4 Conclusion

In this work we numerically studied the real-time dynamics and spectral features of a single hole in the 2D t - J model at finite temperature.

We observed that a three-stage process of hole motion is valid even at finite temperature. In the strong coupling limit, i.e. $t/J \gg 1$, we observe that the speed of hole spreading decreases with temperature at long times. This is in contrast to what would be expected from the mean-field parton theory at $T = 0$ and suggests that the long time spreading is not solely dependent on the spin coupling J .

Furthermore, our findings reveal that, at finite temperature, the initial stage of hole motion is solely dependent on the hopping t . Moreover, for all values of t/J an increase in T results in the prolongation of the initial stage of hole motion.

Contrary to the mean-field parton theory at $T = 0$ one does not observe a hole velocity with a proportionality only dependent on spin coupling J for times larger $1/J$. This is the case already at temperatures $T = 0.5J$ and above. This should also be an incentive to further enhance the mean-field parton theory in order to accurately capture the reported finite temperature behaviour.

Furthermore, in the strong coupling regime there exists a remarkably good agreement with subdiffusive behaviour at high temperatures going down to $T = 2J$. Since our tensor networks calculations were performed on a finite size cylinder it is challenging to observe clean diffusion. Therefore it would be interesting to see whether this behaviour can be confirmed for even larger systems in the future.

We also reported the presence of magnetic polaron peaks up to $T \approx 0.99J$. Note that this is consistent with the temperature up to which non-vanishing local AFM correlations are present at long times. This is an important observation, since it implies that magnetic polarons are robust with respect to temperature. Furthermore, we find that their dispersion relations remain qualitatively unchanged with temperature in the region outside (π, π) as long as magnetic polarons are present.

Finally, we observe nonzero spectral weight and even indications of spin-charge separation around (π, π) for temperatures larger $T = 0.5J$. This is in contrast to the $T = 0$ behaviour, which exhibited a strong suppression of spectral weight in that region. Nevertheless, in order to confirm the spin-charge separation and shed more light on the nature of this phenomenon, further investigation is recommended.

Another highly interesting direction for future research would be the investigation of finite doping, e.g. the case of two holes. At $T = 0$, both a highly mobile bound pair with a dispersion proportional to t and a heavy pair, which moves due to spin exchange processes, have been found [110]. It will be exciting to see whether similar features can be confirmed at finite temperature and to increase our understanding of the pairing mechanism in cuprates.

Our work provides guidance for ultracold atom experiments, which are capable of studying individual magnetic polarons at finite temperature in both real and frequency space. It will therefore be fascinating to see whether a systematic experimental study of the temperature dependence will yield comparable results.

Acknowledgements

This thesis would not have been possible without the support and encouragement of a number of people. First of all, I would like to thank my supervisor Prof. Jan von Delft for the opportunity to do research in his group. His passion for driving physics forward creates a stimulating environment for doing physics and is always a source of great inspiration.

I am grateful for the opportunity to collaborate with Prof. Annabelle Bordth and Prof. Fabian Grusdt, who guided my research with their expertise and knowledge. Without their contribution, my research would not have become what it is.

Special thanks to my main mentor Markus Scheb, who was always open for discussions and tried to support me as much as possible. You have probably invested the most time and energy of all the people listed here in trying to support me and I am very grateful for that.

Thanks also to Andreas for providing a constant stream of ideas that kept my work moving forward.

I would like to thank all the group members who supported me with helpful discussions and made this year an enjoyable experience.

I would also like to thank Sebastian Paeckel for the helpful discussions that improved my understanding of tensor networks.

Last but not least, I would like to thank my friends and family for their continuous support and understanding.

A Spectral function

In Figs. 26 and 27 we present additional results for the spectral function using different t/J .

A.1 Symmetrization

The vertical cuts in Fig. 21 were obtained via the use of symmetrization [54]. Prior to Fourier transformation, the array of the time-dependent correlation data, which is of size $L_x \times L_y$, is reshaped into an array of size $L_y \times L_x$. As a consequence of the reshaping of the array, the momenta transform as

$$k_x \rightarrow k_y \tag{106}$$

$$k_y \rightarrow k_x, \tag{107}$$

effectively resulting in the Fourier transformation being unaltered by the reshaping. It is important to note that this procedure yields an enhanced resolution in the k_y direction.

B Spin correlations in equilibrium

Given that spin correlations are required for the existence of a finite string tension, it is instructive to observe the presence of spin correlations in equilibrium. In Fig. 24 we present the evolution of nearest and next-nearest neighbor spin correlations in equilibrium as a function of temperature.

C Convergence

The results presented in the main text have been subjected to meticulous analysis with regard to convergence in a number of parameters, including the bond dimension D , see Fig. 25.

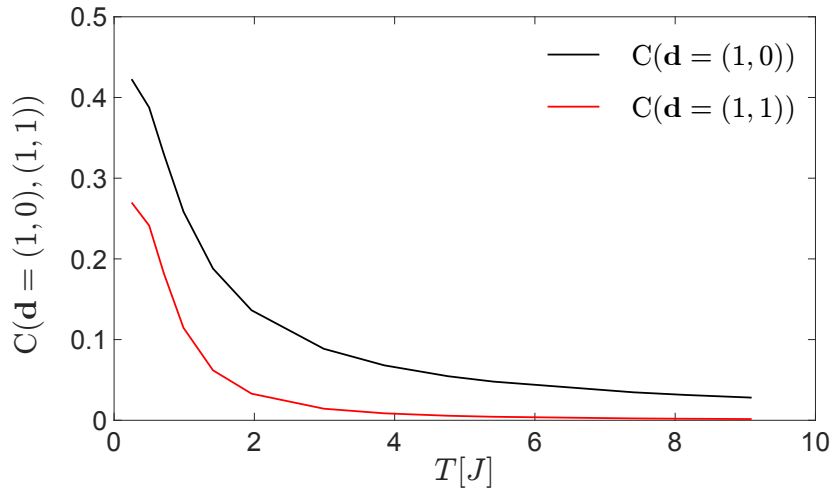


Figure 24: Sign-corrected spin correlations $C_r(\mathbf{d})$ in equilibrium as a function of temperature. The data presented herewith concerns the same t - j cylinder as that discussed in the main text and shows data corresponding to the nearest and next-nearest neighbor case.

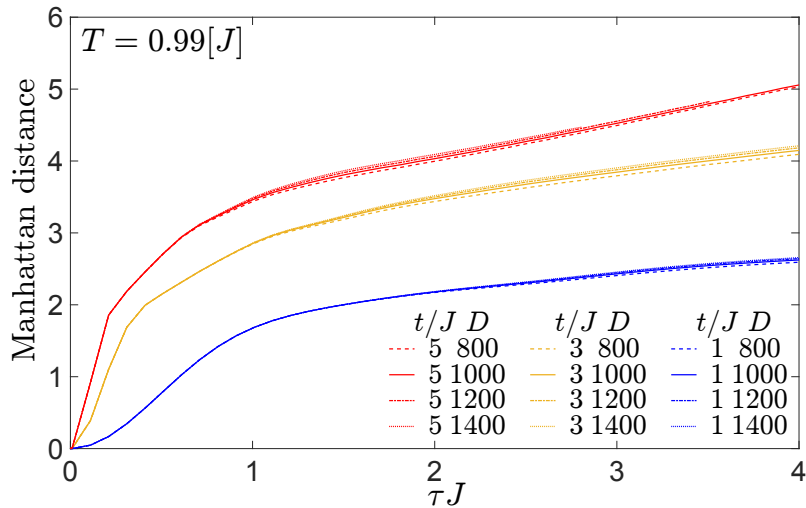


Figure 25: Convergence with bond dimension D in the Manhattan distance at $T = 0.99J$ for $t/J = 1, 3, 5$.

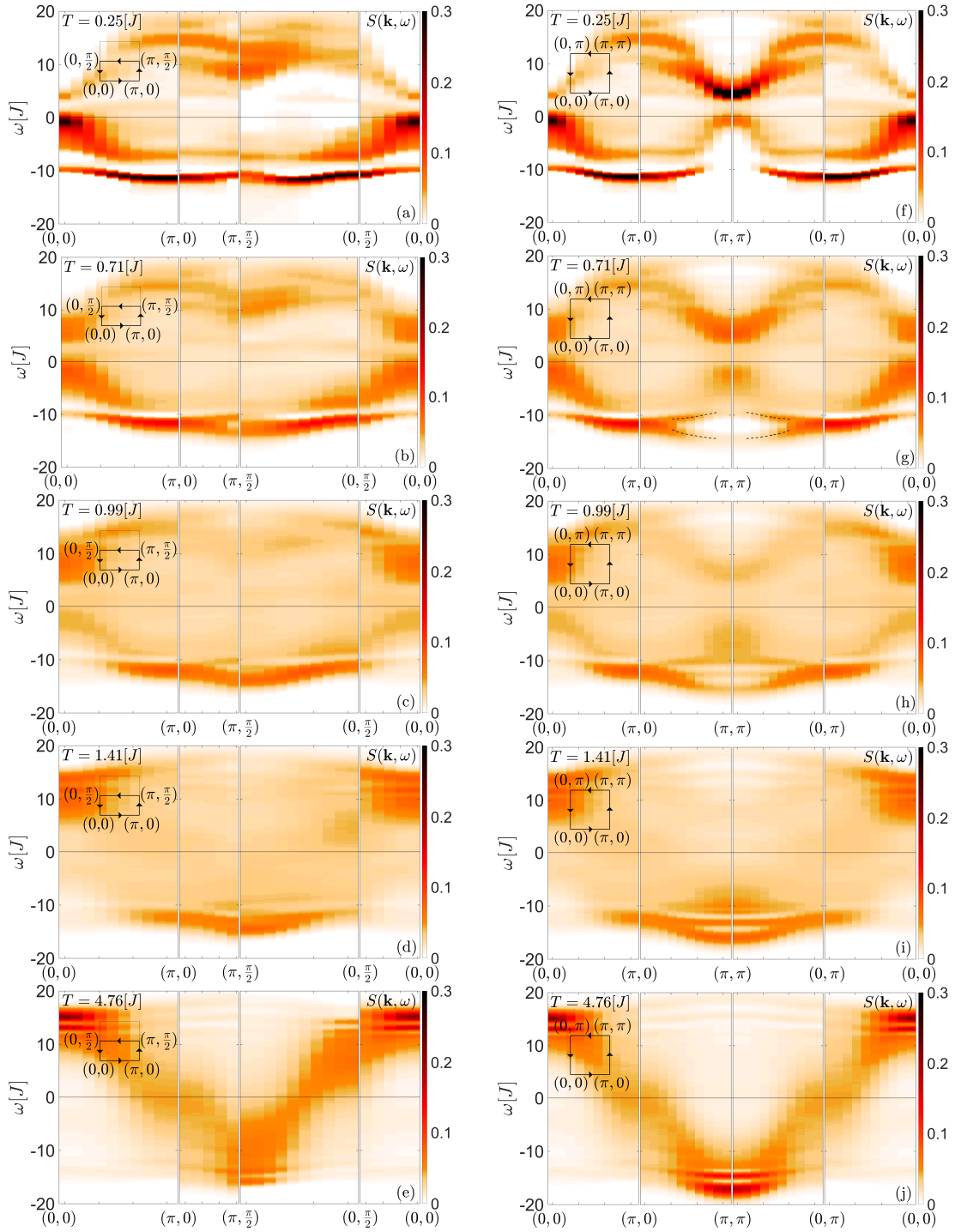


Figure 26: Spectral function calculated in the same manner as Fig. 21 in the main text, but now for $t/J = 5$.

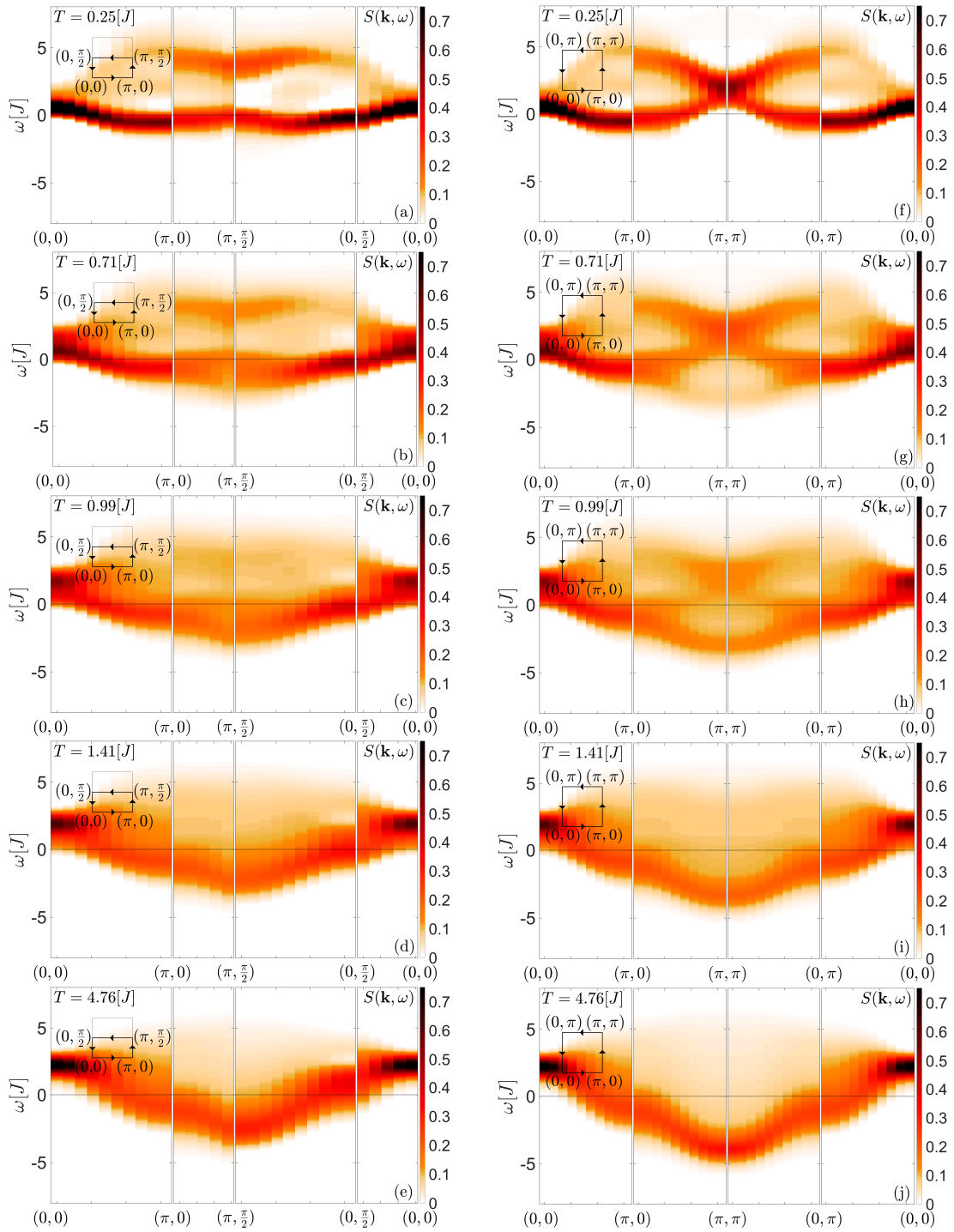


Figure 27: Spectral function calculated in the same manner as Fig. 21 in the main text, but now for $t/J = 1$.

References

- [1] Paul Adrien Maurice Dirac. The quantum theory of the electron. *Proceedings of the Royal Society of London. Series A, Containing Papers of a Mathematical and Physical Character*, 117(778):610–624, 1928.
- [2] LD Landau. On the theory of the fermi liquid. *Sov. Phys. JETP*, 8(1):70, 1959.
- [3] Elbio Dagotto. Correlated electrons in high-temperature superconductors. *Reviews of Modern Physics*, 66(3):763, 1994.
- [4] Philip W Anderson. *The theory of superconductivity in the high- T_c cuprate superconductors*. 1997.
- [5] Horst L Stormer. Nobel lecture: the fractional quantum hall effect. *Reviews of Modern Physics*, 71(4):875, 1999.
- [6] Alexander Weiße and Holger Fehske. Exact diagonalization techniques. *Computational many-particle physics*, pages 529–544, 2008.
- [7] G Sugiyama and SE Koonin. Auxiliary field monte-carlo for quantum many-body ground states. *Annals of Physics*, 168(1):1–26, 1986.
- [8] Emanuel Gull, Andrew J Millis, Alexander I Lichtenstein, Alexey N Rubtsov, Matthias Troyer, and Philipp Werner. Continuous-time monte carlo methods for quantum impurity models. *Reviews of Modern Physics*, 83(2):349–404, 2011.
- [9] William MC Foulkes, Lubos Mitas, RJ Needs, and Guna Rajagopal. Quantum monte carlo simulations of solids. *Reviews of Modern Physics*, 73(1):33, 2001.
- [10] Matthias Troyer and Uwe-Jens Wiese. Computational complexity and fundamental limitations to fermionic quantum monte carlo simulations. *Physical review letters*, 94(17):170201, 2005.
- [11] Gaopei Pan and Zi Yang Meng. Sign problem in quantum monte carlo simulation. *arXiv preprint arXiv:2204.08777*, 2022.
- [12] Ulrich Schollwöck. The density-matrix renormalization group in the age of matrix product states. *Annals of physics*, 326(1):96–192, 2011.
- [13] Jens Eisert. Entanglement and tensor network states. *arXiv preprint arXiv:1308.3318*, 2013.
- [14] Román Orús. A practical introduction to tensor networks: Matrix product states and projected entangled pair states. *Annals of physics*, 349:117–158, 2014.

REFERENCES

- [15] Steven R White. Density matrix formulation for quantum renormalization groups. *Physical review letters*, 69(19):2863, 1992.
- [16] Steven R White. Density-matrix algorithms for quantum renormalization groups. *Physical review b*, 48(14):10345, 1993.
- [17] Patrick A. Lee, Naoto Nagaosa, and Xiao-Gang Wen. Doping a mott insulator: Physics of high-temperature superconductivity. *Rev. Mod. Phys.*, 78:17–85, Jan 2006.
- [18] F. Grusdt, M. Kánasz-Nagy, A. Bohrdt, C. S. Chiu, G. Ji, M. Greiner, D. Greif, and E. Demler. Parton theory of magnetic polarons: Mesonic resonances and signatures in dynamics. *Phys. Rev. X*, 8:011046, Mar 2018.
- [19] C Kim, AY Matsuura, Z-X Shen, N Motoyama, H Eisaki, S Uchida, Takami Tohyama, and S Maekawa. Observation of spin-charge separation in one-dimensional srco o 2. *Physical review letters*, 77(19):4054, 1996.
- [20] C Kim, Z-X Shen, N Motoyama, H Eisaki, S Uchida, T Tohyama, and S Maekawa. Separation of spin and charge excitations in one-dimensional srco 2. *Physical Review B*, 56(24):15589, 1997.
- [21] Michael Sing, Udo Schwingenschlögl, Ralph Claessen, Peter Blaha, JMP Carmelo, LM Martelo, PD Sacramento, Martin Dressel, and Claus Schelde Jacobsen. Electronic structure of the quasi-one-dimensional organic conductor ttf-tcnq. *Physical Review B*, 68(12):125111, 2003.
- [22] JM Luttinger. An exactly soluble model of a many-fermion system. *Journal of mathematical physics*, 4(9):1154–1162, 1963.
- [23] Elliott H Lieb and Fa-Yueh Wu. Absence of mott transition in an exact solution of the short-range, one-band model in one dimension. *Physical Review Letters*, 20(25):1445, 1968.
- [24] Masao Ogata and Hiroyuki Shiba. Bethe-ansatz wave function, momentum distribution, and spin correlation in the one-dimensional strongly correlated hubbard model. *Physical Review B*, 41(4):2326, 1990.
- [25] KJ Von Szczepanski, P Horsch, W Stephan, and M Ziegler. Single-particle excitations in a quantum antiferromagnet. *Physical Review B*, 41(4):2017, 1990.
- [26] ZY Weng, DN Sheng, and CS Ting. Spin-charge separation in the t-j model: Magnetic and transport anomalies. *Physical Review B*, 52(1):637, 1995.
- [27] RN Bannister and N d’Ambrumenil. Spectral functions of half-filled one-dimensional hubbard rings with varying boundary conditions. *Physical Review B*, 61(7):4651, 2000.

REFERENCES

- [28] Thierry Giamarchi. *Quantum physics in one dimension*, volume 121. Clarendon press, 2003.
- [29] BO Wells, Z-X Shen, A Matsuura, DM King, MA Kastner, M Greven, and RJ Birgeneau. E versus k relations and many body effects in the model insulating copper oxide $\text{Sr}_2\text{CuO}_2\text{Cl}_2$. *Physical review letters*, 74(6):964, 1995.
- [30] F Ronning, KM Shen, NP Armitage, A Damascelli, DH Lu, Z-X Shen, LL Miller, and C Kim. Anomalous high-energy dispersion in angle-resolved photoemission spectra from the insulating cuprate $\text{Ca}_2\text{CuO}_2\text{Cl}_2$. *Physical Review B—Condensed Matter and Materials Physics*, 71(9):094518, 2005.
- [31] J Graf, G-H Gweon, K McElroy, SY Zhou, C Jozwiak, E Rotenberg, A Bill, T Sasagawa, H Eisaki, S Uchida, et al. Universal high energy anomaly in the angle-resolved photoemission spectra of high temperature superconductors: possible evidence of spinon and holon branches. *Physical review letters*, 98(6):067004, 2007.
- [32] S Schmitt-Rink, CM Varma, and AE Ruckenstein. Spectral function of holes in a quantum antiferromagnet. *Physical review letters*, 60(26):2793, 1988.
- [33] CL Kane, PA Lee, and N Read. Motion of a single hole in a quantum antiferromagnet. *Physical Review B*, 39(10):6880, 1989.
- [34] Subir Sachdev. Hole motion in a quantum néel state. *Physical Review B*, 39(16):12232, 1989.
- [35] Veit Elser, David A Huse, Boris I Shraiman, and Eric D Siggia. Ground state of a mobile vacancy in a quantum antiferromagnet: Small-cluster study. *Physical Review B*, 41(10):6715, 1990.
- [36] Elbio Dagotto, Robert Joynt, Adriana Moreo, Silvia Bacci, and Eduardo Gagliano. Strongly correlated electronic systems with one hole: Dynamical properties. *Physical Review B*, 41(13):9049, 1990.
- [37] Gerardo Martinez and Peter Horsch. Spin polarons in the t-j model. *Physical Review B*, 44(1):317, 1991.
- [38] Assa Auerbach and Brond E Larson. Small-polaron theory of doped antiferromagnets. *Physical review letters*, 66(17):2262, 1991.
- [39] Zhiping Liu and Efstratios Manousakis. Dynamical properties of a hole in a heisenberg antiferromagnet. *Physical Review B*, 45(5):2425, 1992.
- [40] Massimo Boninsegni and Efstratios Manousakis. Green’s-function monte carlo study of the t-j model. *Physical Review B*, 46(1):560, 1992.

REFERENCES

- [41] Massimo Boninsegni and Efstratios Manousakis. Variational description of a quasihole excitation in a quantum antiferromagnet. *Physical Review B*, 45(9):4877, 1992.
- [42] Pak Wo Leung and Robert J Gooding. Dynamical properties of the single-hole t-j model on a 32-site square lattice. *Physical Review B*, 52(22):R15711, 1995.
- [43] Oleg A Starykh, Oziel F de Alcantara Bonfim, and George F Reiter. Self-consistent born approximation for the hole motion in the three-band model: a comparison with photoemission experiments. *Physical Review B*, 52(17):12534, 1995.
- [44] Michael Brunner, Fakhre F Assaad, and Alejandro Muramatsu. Single-hole dynamics in the t-j model on a square lattice. *Physical Review B*, 62(23):15480, 2000.
- [45] AS Mishchenko, NV Prokof'ev, and BV Svistunov. Single-hole spectral function and spin-charge separation in the t-j model. *Physical Review B*, 64(3):033101, 2001.
- [46] Steven R White and Ian Affleck. Density matrix renormalization group analysis of the nagaoka polaron in the two-dimensional t-j model. *Physical Review B*, 64(2):024411, 2001.
- [47] G Sangiovanni, A Toschi, E Koch, K Held, Massimo Capone, Claudio Castellani, O Gunnarsson, S-K Mo, JW Allen, H-D Kim, et al. Static versus dynamical mean-field theory of mott antiferromagnets. *Physical Review B—Condensed Matter and Materials Physics*, 73(20):205121, 2006.
- [48] Efstratios Manousakis. String excitations of a hole in a quantum antiferromagnet and photoelectron spectroscopy. *Physical Review B—Condensed Matter and Materials Physics*, 75(3):035106, 2007.
- [49] Fabio Mezzacapo. Variational study of a mobile hole in a two-dimensional quantum antiferromagnet using entangled-plaquette states. *Physical Review B—Condensed Matter and Materials Physics*, 83(11):115111, 2011.
- [50] Joannis Koepsell, Jayadev Vijayan, Pimonpan Sompert, Fabian Grusdt, Timon A Hilker, Eugene Demler, Guillaume Salomon, Immanuel Bloch, and Christian Gross. Imaging magnetic polarons in the doped fermi-hubbard model. *Nature*, 572(7769):358–362, 2019.
- [51] Fabian Grusdt, Annabelle Bohrdt, and Eugene Demler. Microscopic spinon-chargon theory of magnetic polarons in the t-j model. *Physical Review B*, 99(22):224422, 2019.

- [52] T Cuk, DH Lu, XJ Zhou, Z-X Shen, TP Devereaux, and N Nagaosa. A review of electron–phonon coupling seen in the high- t_c superconductors by angle-resolved photoemission studies (arpes). *physica status solidi (b)*, 242(1):11–29, 2005.
- [53] Annabelle Bohrdt, Fabian Grusdt, and Michael Knap. Dynamical formation of a magnetic polaron in a two-dimensional quantum antiferromagnet. *New Journal of Physics*, 22(12):123023, 2020.
- [54] Annabelle Bohrdt, Eugene Demler, Frank Pollmann, Michael Knap, and Fabian Grusdt. Parton theory of angle-resolved photoemission spectroscopy spectra in antiferromagnetic mott insulators. *Physical Review B*, 102(3):035139, 2020.
- [55] Daniel Greif, Thomas Uehlinger, Gregor Jotzu, Leticia Tarruell, and Tilman Esslinger. Short-range quantum magnetism of ultracold fermions in an optical lattice. *Science*, 340(6138):1307–1310, 2013.
- [56] Russell A Hart, Pedro M Duarte, Tsung-Lin Yang, Xinxing Liu, Thereza Paiva, Ehsan Khatami, Richard T Scalettar, Nandini Trivedi, David A Huse, and Randall G Hulet. Observation of antiferromagnetic correlations in the hubbard model with ultracold atoms. *Nature*, 519(7542):211–214, 2015.
- [57] Maxwell F Parsons, Florian Huber, Anton Mazurenko, Christie S Chiu, Widagdo Setiawan, Katherine Wooley-Brown, Sebastian Blatt, and Markus Greiner. Site-resolved imaging of fermionic li 6 in an optical lattice. *Physical review letters*, 114(21):213002, 2015.
- [58] Lawrence W Cheuk, Matthew A Nichols, Katherine R Lawrence, Melih Okan, Hao Zhang, Ehsan Khatami, Nandini Trivedi, Thereza Paiva, Marcos Rigol, and Martin W Zwierlein. Observation of spatial charge and spin correlations in the 2d fermi-hubbard model. *Science*, 353(6305):1260–1264, 2016.
- [59] Anton Mazurenko, Christie S Chiu, Geoffrey Ji, Maxwell F Parsons, Márton Kanász-Nagy, Richard Schmidt, Fabian Grusdt, Eugene Demler, Daniel Greif, and Markus Greiner. A cold-atom fermi–hubbard antiferromagnet. *Nature*, 545(7655):462–466, 2017.
- [60] Timon A Hilker, Guillaume Salomon, Fabian Grusdt, Ahmed Omran, Martin Boll, Eugene Demler, Immanuel Bloch, and Christian Gross. Revealing hidden antiferromagnetic correlations in doped hubbard chains via string correlators. *Science*, 357(6350):484–487, 2017.
- [61] Peter T Brown, Debayan Mitra, Elmer Guardado-Sanchez, Reza Nourafkan, Alexis Reymbaut, Charles-David Hébert, Simon Bergeron, A-MS Tremblay, Jure Kokalj, David A Huse, et al. Bad metallic transport in a cold atom fermi-hubbard system. *Science*, 363(6425):379–382, 2019.

- [62] Matthew A Nichols, Lawrence W Cheuk, Melih Okan, Thomas R Hartke, Enrique Mendez, T Senthil, Ehsan Khatami, Hao Zhang, and Martin W Zwierlein. Spin transport in a mott insulator of ultracold fermions. *Science*, 363(6425):383–387, 2019.
- [63] Guillaume Salomon, Joannis Koepsell, Jayadev Vijayan, Timon A Hilker, Jacopo Nespolo, Lode Pollet, Immanuel Bloch, and Christian Gross. Direct observation of incommensurate magnetism in hubbard chains. *Nature*, 565(7737):56–60, 2019.
- [64] Christie S Chiu, Geoffrey Ji, Annabelle Bohrdt, Muqing Xu, Michael Knap, Eugene Demler, Fabian Grusdt, Markus Greiner, and Daniel Greif. String patterns in the doped hubbard model. *Science*, 365(6450):251–256, 2019.
- [65] P Béran, D Poilblanc, and RB Laughlin. Evidence for composite nature of quasiparticles in the 2d tj model. *Nuclear Physics B*, 473(3):707–720, 1996.
- [66] Bastien Dalla Piazza, M Mourigal, Niels Bech Christensen, GJ Nilsen, P Tregenna-Piggott, TG Perring, Mechtild Enderle, Desmond Francis Mc-Morrow, DA Ivanov, and Henrik Moodysson Rønnow. Fractional excitations in the square-lattice quantum antiferromagnet. *Nature physics*, 11(1):62–68, 2015.
- [67] Fabian Grusdt, Zheng Zhu, Tao Shi, and Eugene Demler. Meson formation in mixed-dimensional t-J models. *SciPost Phys.*, 5(6):057, December 2018.
- [68] VJ Emery. Theory of high- t c superconductivity in oxides. *Physical Review Letters*, 58(26):2794, 1987.
- [69] Elbio Dagotto. Correlated electrons in high-temperature superconductors. *Reviews of Modern Physics*, 66(3):763, 1994.
- [70] Patrick A Lee, Naoto Nagaosa, and Xiao-Gang Wen. Doping a mott insulator: Physics of high-temperature superconductivity. *Reviews of modern physics*, 78(1):17–85, 2006.
- [71] Jozef Spalek. tj model then and now: a personal perspective from the pioneering times. *arXiv preprint arXiv:0706.4236*, 2007.
- [72] Peter T Brown, Elmer Guardado-Sanchez, Benjamin M Spar, Edwin W Huang, Thomas P Devereaux, and Waseem S Bakr. Angle-resolved photoemission spectroscopy of a fermi–hubbard system. *Nature Physics*, 16(1):26–31, 2020.
- [73] A. Bohrdt, D. Greif, E. Demler, M. Knap, and F. Grusdt. Angle-resolved photoemission spectroscopy with quantum gas microscopes. *Phys. Rev. B*, 97:125117, Mar 2018.

- [74] Steven R. White. Density matrix formulation for quantum renormalization groups. *Phys. Rev. Lett.*, 69(19):2863–2866, November 1992.
- [75] Steven R. White. Density-matrix algorithms for quantum renormalization groups. *Phys. Rev. B*, 48(14):10345–10356, October 1993.
- [76] A. Nocera and G. Alvarez. Symmetry-conserving purification of quantum states within the density matrix renormalization group. *Phys. Rev. B*, 93:045137, Jan 2016.
- [77] Adrian E. Feiguin and Steven R. White. Finite-temperature density matrix renormalization using an enlarged hilbert space. *Phys. Rev. B*, 72:220401, Dec 2005.
- [78] Adrian E. Feiguin and Gregory A. Fiete. Spectral properties of a spin-incoherent luttinger liquid. *Phys. Rev. B*, 81:075108, Feb 2010.
- [79] Johannes Michael Hauschild. *Quantum Many-Body Systems Far Out of Equilibrium—Simulations with Tensor Networks*. PhD thesis, Technische Universität München, 2019.
- [80] Sebastian Paeckel, Thomas Köhler, Andreas Swoboda, Salvatore R Manmana, Ulrich Schollwöck, and Claudius Hubig. Time-evolution methods for matrix-product states. *Annals of Physics*, 411:167998, 2019.
- [81] Juan José García-Ripoll. Time evolution of Matrix Product States. *New J. Phys.*, 8(12):305, December 2006.
- [82] P. E. Dargel, A. Wöllert, A. Honecker, I. P. McCulloch, U. Schollwöck, and T. Pruschke. Lanczos algorithm with matrix product states for dynamical correlation functions. *Phys. Rev. B*, 85(20):205119, May 2012.
- [83] Michael L. Wall. Out-of-Equilibrium Dynamics with Matrix Product States. In *Quantum Many-Body Physics of Ultracold Molecules in Optical Lattices*, pages 177–222. Springer, Cham, Switzerland, 2015.
- [84] Jutho Haegeman, J Ignacio Cirac, Tobias J Osborne, Iztok Pižorn, Henri Verschelde, and Frank Verstraete. Time-dependent variational principle for quantum lattices. *Physical review letters*, 107(7):070601, 2011.
- [85] Jutho Haegeman, Christian Lubich, Ivan Oseledets, Bart Vandereycken, and Frank Verstraete. Unifying time evolution and optimization with matrix product states. *Phys. Rev. B*, 94:165116, Oct 2016.
- [86] C. Karrasch, J. H. Bardarson, and J. E. Moore. Finite-temperature dynamical density matrix renormalization group and the drude weight of spin-1/2 chains. *Phys. Rev. Lett.*, 108:227206, May 2012.

REFERENCES

- [87] DM Kennes and Christoph Karrasch. Extending the range of real time density matrix renormalization group simulations. *Computer Physics Communications*, 200:37–43, 2016.
- [88] C Karrasch, JH Bardarson, and JE Moore. Reducing the numerical effort of finite-temperature density matrix renormalization group calculations. *New Journal of Physics*, 15(8):083031, 2013.
- [89] Andreas Gleis, Jheng-Wei Li, and Jan Von Delft. Controlled bond expansion for density matrix renormalization group ground state search at single-site costs. *Physical Review Letters*, 130(24):246402, 2023.
- [90] Jheng-Wei Li, Andreas Gleis, and Jan von Delft. Time-dependent variational principle with controlled bond expansion for matrix product states. *Phys. Rev. Lett.*, 133:026401, Jul 2024.
- [91] Andreas Gleis, Jheng-Wei Li, and Jan von Delft. Projector formalism for kept and discarded spaces of matrix product states. *Phys. Rev. B*, 106:195138, Nov 2022.
- [92] J. Eisert, M. Cramer, and M. B. Plenio. Colloquium: Area laws for the entanglement entropy. *Rev. Mod. Phys.*, 82:277–306, Feb 2010.
- [93] J. Ignacio Cirac, David Pérez-García, Norbert Schuch, and Frank Verstraete. Matrix product states and projected entangled pair states: Concepts, symmetries, theorems. *Rev. Mod. Phys.*, 93:045003, Dec 2021.
- [94] Matthew B Hastings. An area law for one-dimensional quantum systems. *Journal of statistical mechanics: theory and experiment*, 2007(08):P08024, 2007.
- [95] Michael L Wall and Michael L Wall. Out-of-equilibrium dynamics with matrix product states. *Quantum Many-Body Physics of Ultracold Molecules in Optical Lattices: Models and Simulation Methods*, pages 177–222, 2015.
- [96] Gene H Golub and Charles F Van Loan. Matrix computations, johns hopkins u. *Math. Sci., Johns Hopkins University Press, Baltimore, MD*, 1996.
- [97] F. Verstraete, J. J. García-Ripoll, and J. I. Cirac. Matrix product density operators: Simulation of finite-temperature and dissipative systems. *Phys. Rev. Lett.*, 93:207204, Nov 2004.
- [98] Steven R. White. Minimally entangled typical quantum states at finite temperature. *Phys. Rev. Lett.*, 102:190601, May 2009.
- [99] Gregory M. Crosswhite and Dave Bacon. Finite automata for caching in matrix product algorithms. *Phys. Rev. A*, 78:012356, Jul 2008.

REFERENCES

- [100] Gregory M. Crosswhite, A. C. Doherty, and Guifré Vidal. Applying matrix product operators to model systems with long-range interactions. *Phys. Rev. B*, 78:035116, Jul 2008.
- [101] Markus Scheb. Variational optimization of finite projected entangled pair states. 2021.
- [102] G. Ehlers, S. R. White, and R. M. Noack. Hybrid-space density matrix renormalization group study of the doped two-dimensional hubbard model. *Phys. Rev. B*, 95:125125, Mar 2017.
- [103] JE Hopcroft. Introduction to automata theory, languages, and computation, 2001.
- [104] Kaijun Shen, Kewei Sun, Maxim F Gelin, and Yang Zhao. Finite-temperature hole–magnon dynamics in an antiferromagnet. *The Journal of Physical Chemistry Letters*, 15(2):447–453, 2024.
- [105] Geoffrey Ji, Muqing Xu, Lev Haldar Kendrick, Christie S. Chiu, Justus C. Brüggengjürgen, Daniel Greif, Annabelle Bohrdt, Fabian Grusdt, Eugene Demler, Martin Lebrat, and Markus Greiner. Coupling a mobile hole to an antiferromagnetic spin background: Transient dynamics of a magnetic polaron. *Phys. Rev. X*, 11:021022, Apr 2021.
- [106] B Jackson Leland. *DIGITAL FILTERS AND SIGNAL PROCESSING*. KLUWER ACADEMIC PUBLISHERS., 1989.
- [107] Ruben Verresen, Frank Pollmann, and Roderich Moessner. Quantum dynamics of the square-lattice heisenberg model. *Physical Review B*, 98(15):155102, 2018.
- [108] Steven R. White and Ian Affleck. Density matrix renormalization group analysis of the nagaoka polaron in the two-dimensional $t - j$ model. *Phys. Rev. B*, 64:024411, Jun 2001.
- [109] Lauritz Hahn, Annabelle Bohrdt, and Fabian Grusdt. Dynamical signatures of thermal spin-charge deconfinement in the doped ising model. *Phys. Rev. B*, 105:L241113, Jun 2022.
- [110] Annabelle Bohrdt, Eugene Demler, and Fabian Grusdt. Dichotomy of heavy and light pairs of holes in the $t - j$ model. *Nature Communications*, 14(1):8017, 2023.

Declaration

I hereby declare that this thesis is my own work, and that I have not used any sources and aids other than those stated in the thesis.

München, November 29, 2024

(Toni Guthardt)

Lebenslauf

Persönliche Daten

Name Toni Benedikt Guthardt
Anschrift Reutbergstraße 29a
83666 Waakirchen
Tel. 08021/90639
E-Mail toni.guthardt@isnil.de
Geb. 19.07.1999 in Schaftlach
Eltern Vater: Dieter Guthardt | Mutter: Christel Guthardt

Schulische Ausbildung

2006 – 2010: Grundschule Waakirchen
2010 – 2018: Gabriel-von-Seidl-Gymnasium Bad Tölz
Abschluss mit Allgemeiner Hochschulreife

Studium an Hochschulen

2018 – 2022 Studium B.Sc. Physik an der LMU in München
Abschluss mit Bachelor of Science
2022 – Studium M.Sc. Physik an der LMU in München

Außerberufliche Weiterbildung

07/15: **Betriebspraktikum als Fachinformatiker Systemintegration**
im Fraunhofer-Institut für Bauphysik in Holzkirchen
11/15: **Teilnahme an der internationalen MUN Konferenz** in
München
03/16: **Teilnahme an der internationalen MUN Konferenz** in
Amsterdam
03/17 **Teilnahme an der internationalen MUN Konferenz** in
Edinburgh
04/18 **Teilnahme an der internationalen MUN Konferenz** in
Amsterdam

Besondere Kenntnisse und Fähigkeiten

Englisch: fortgeschrittene Sprachkenntnisse aufgrund schulischer Bildung
(Sprachniveau C1) und privater Weiterbildung, ausreichend für
anspruchsvolle Konversation und Debatten.

Waakirchen, den 22.11.2024



Toni Guthardt